$$\varepsilon = \ln(1 + \varepsilon_E) \tag{4.4}$$

The above conversions assume incompressible, homogeneous deformation. Figure 4.2 shows the uniaxial (tensile) stress-strain curve for the 'bi-linear' plasticity material model.

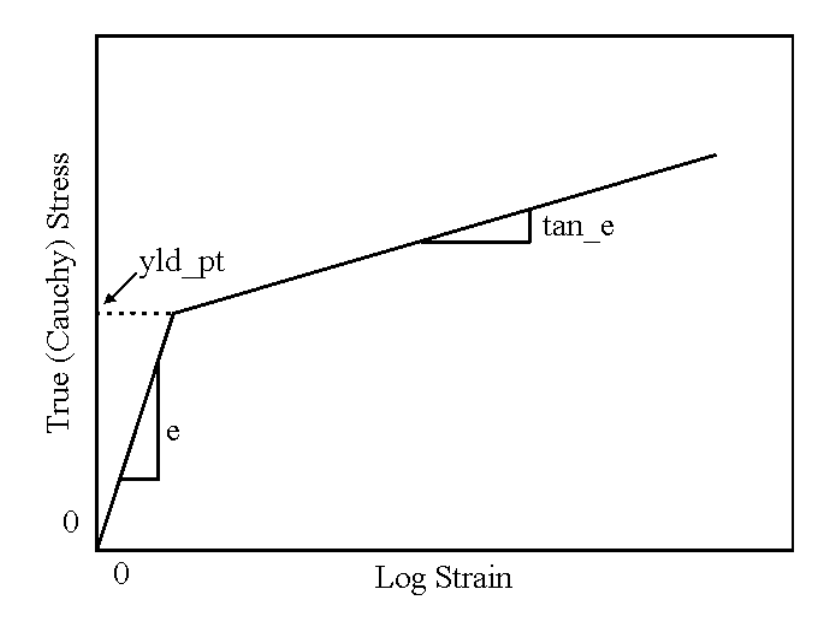


Figure 4.2: Uniaxial (tensile) stress-strain curve for the 'bi-linear' plasticity material

Mesh Generation and Applied Loading

All the pre-processing part of the model was executed using the finite element pre-processing package PATRAN v9.0 [15]. Figure 4.3 shows typical finite element meshes developed in this study. The meshes consisted of three dimensional linear bricks i.e. C3D8 available in ABAQUS (HKS 1998) and l3disop available in WARP3D. Due to the symmetry condition, only one quarter of the specimens was modelled. In order to save the analyses times, coarse meshes were used to model the specimen. The model contained one layer in the Z direction. A sharp crack was modelled at the crack tip. The nodes at the crack tip were tied together in elastic analysis. Collapsed elements was used to model the crack tip for elastic-

plastic analysis. To check the theory that J-integral should be path independent, four contours were chosen for J-integral calculations.

Uniform stress was applied linearly from zero up to 68.9 MPa within 5×10^{-6} seconds and held constant until 10×10^{-6} seconds. The results from WARP3D were compared with the results from ABAQUS.

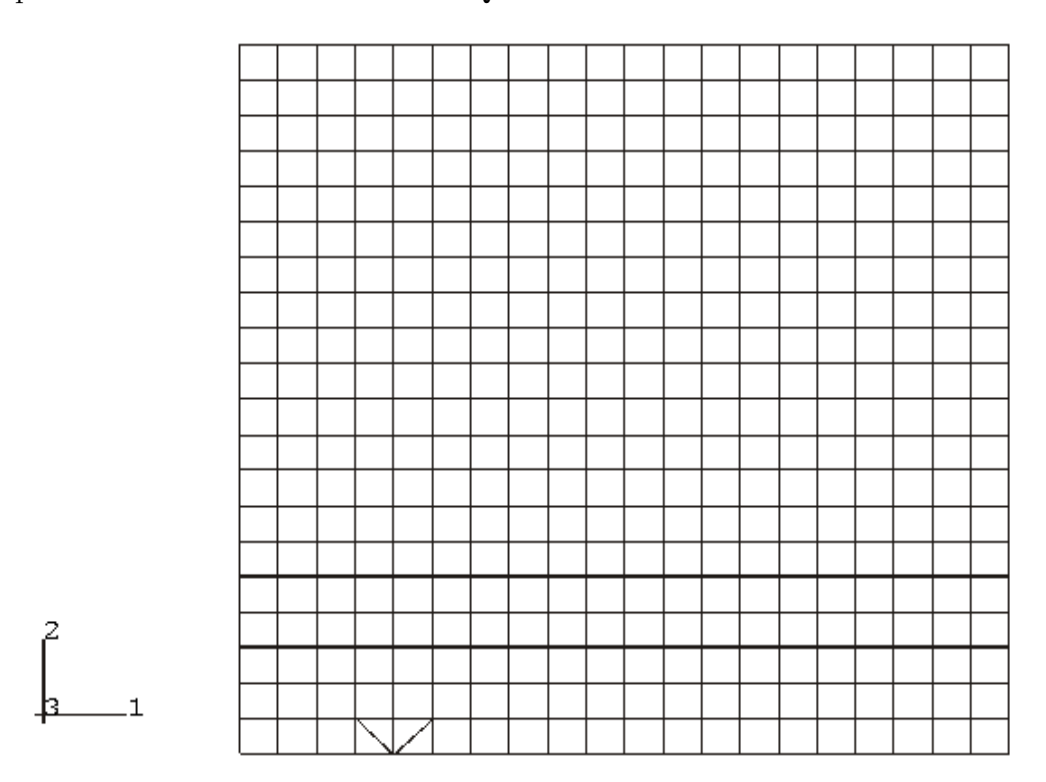


Figure 4.3: Finite element model of a cracked plate

4.2.2 Ramp Loading on Cracked Bend Specimen

The finite element analyses also involved three dimensional J-integral calculations for the three point bend (TPB) fracture toughness specimen of steel subjected to rapid ramp loading. The geometry of the TPB specimen was chosen from BS6729 [6]. A standard TPB specimen has dimensions 200 mm long x 50 mm width x 25 mm thick as shown in Figure 4.4. The plane strain specimen is a beam with a single edge notch at one edge leaving an uncracked ligament of the rest of the width. Taking advantage of symmetry about X = 0, one-half of the specimen was

modelled as shown in Figure 4.5. The boundary conditions were restrained from movement in the x-direction for all the nodes in the axis of symmetry and the node at the support was restrained from movement in the y-direction.

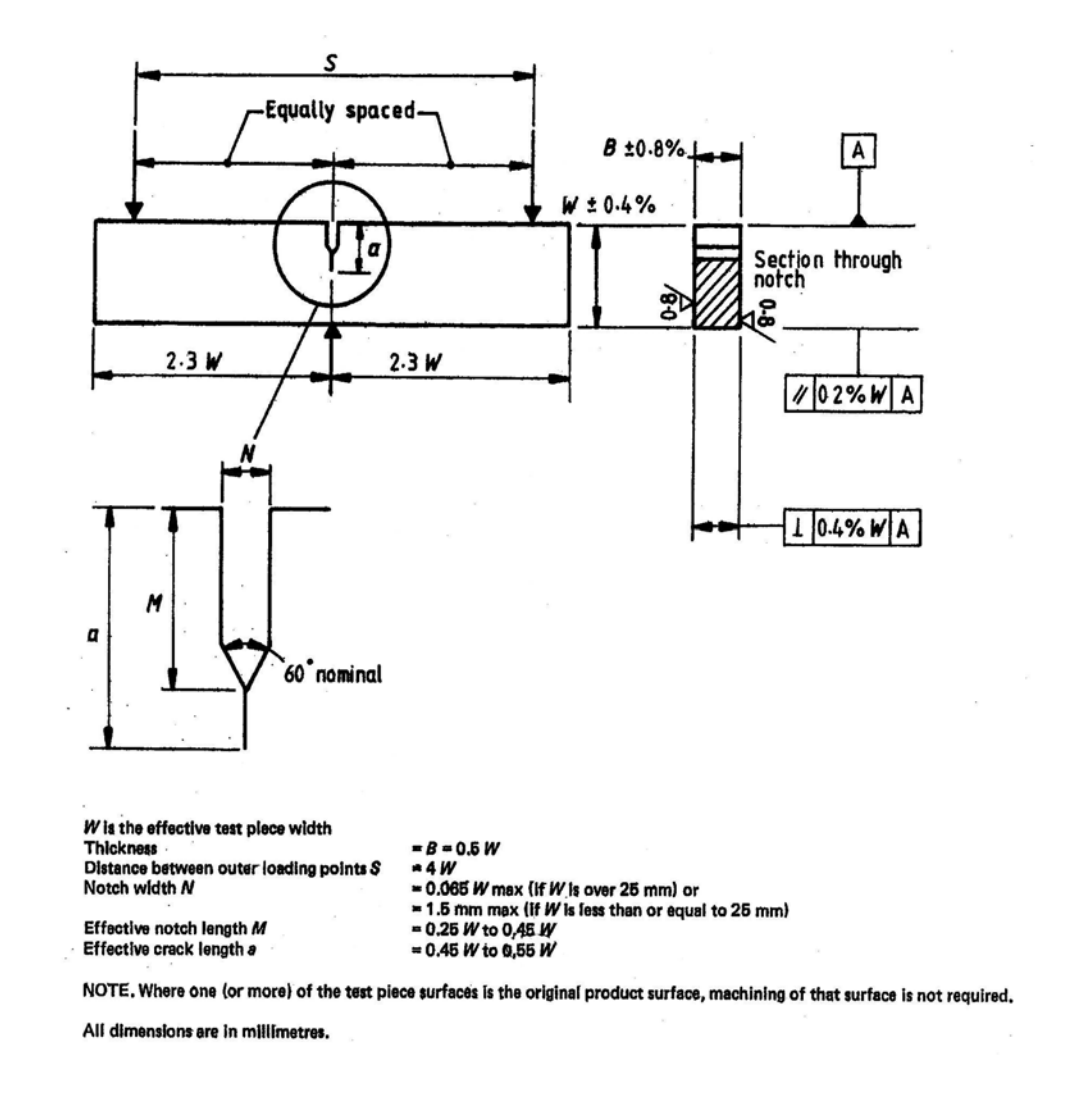


Figure 4.4: Proportional dimensions and tolerances for test TPB specimen [6]

Mesh Generation

PATRAN v9.0 was used to create the input model of the specimens. At the area around the crack tip, there are two layers of the mesh as shown in Figure 4.6. At a small, region, approximately less than ten times the crack tip opening, a fine mesh was modelled to ensure accuracy of the results. In a large strain analysis, an

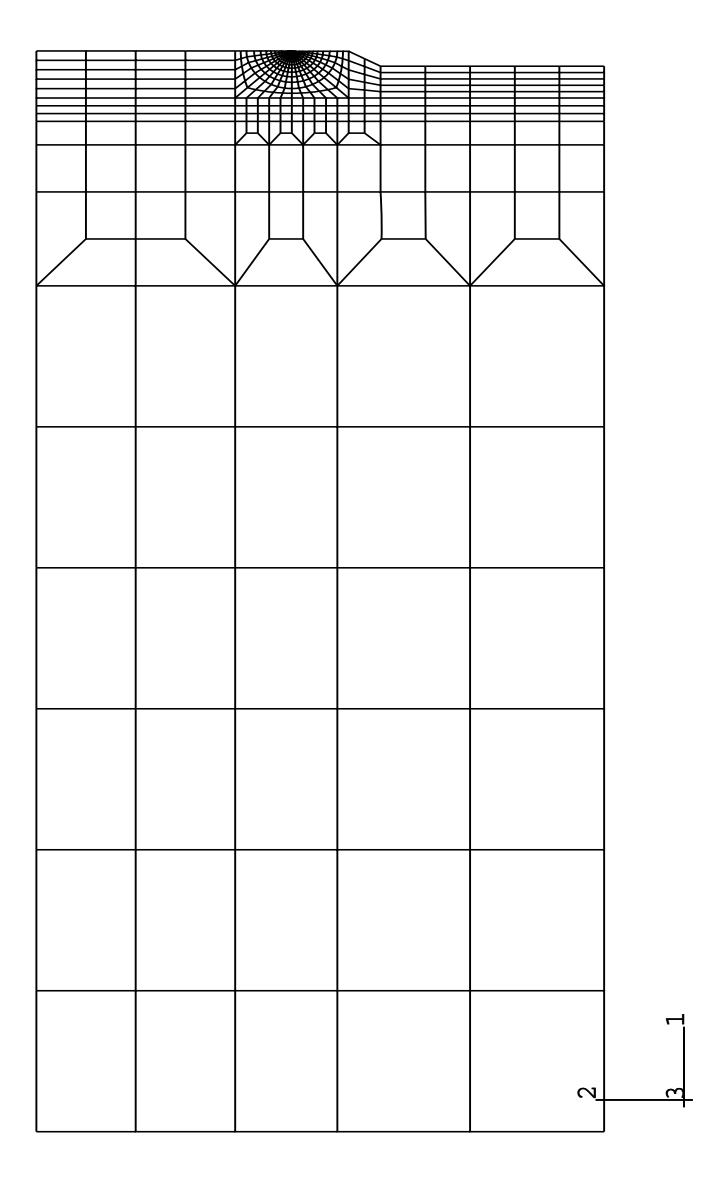


Figure 4.5: Finite element model of half TPB specimen

absolute sharp crack tip should not be adopted. Therefore an initial small notch radius was defined at 0.03 mm. There was one layer of elements in the full thickness. The finite element analyses employed 3D isoparametric elements (i.e. element type C3D8 available in ABAQUS (HKS 1998) and l3disop available in WARP3D. At the area around the crack tip, there were 20 contours in order to extract accurate J-integral values.

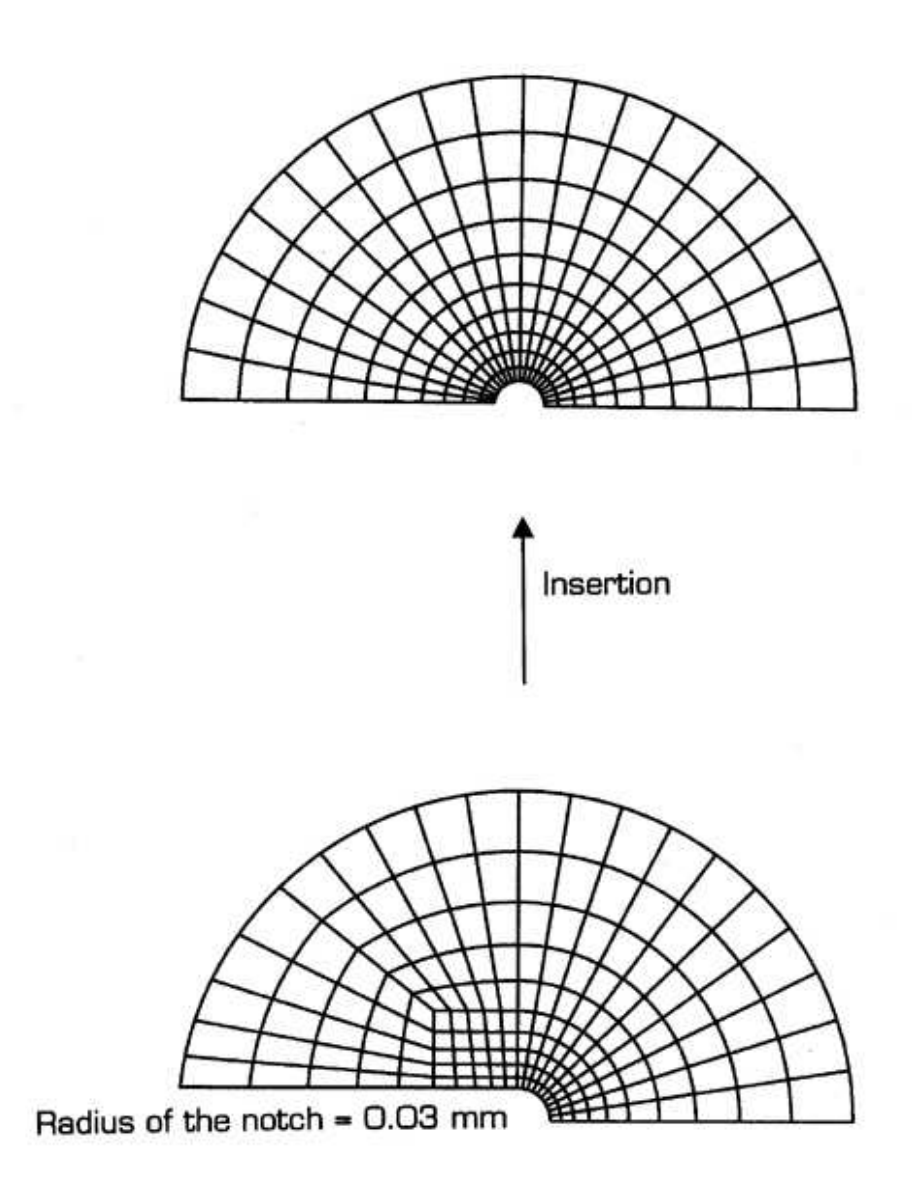


Figure 4.6: Finite element meshes in the crack tip region

Material Properties and Applied Loading

The material model for this analysis was based on the incremental plasticity theory with the Von Mises yield criterion. The material was assumed to be bi-linear with strain hardening slope. The yield stress was assumed to be 350 MPa and Young's modulus 210 GPa. Strain hardening was assumed to be isotropic with slope 21 GPa.

Applied loading was assumed to be linear and within the ranges of inertia effects. The loads were applied linearly from zero up to a chosen maximum load of 20 kN within 0.01421 seconds when loading was stopped.

Finite Element Analysis

The finite element software packages, WARP3D and ABAQUS, were used for the numerical computational analysis. Details of each software used in this study are described below:

ABAQUS The general direct time integration method, called the Hilber-Hugues-Taylor operator, provided in ABAQUS/standard was used in the dynamic response analyses. The set of simultaneous nonlinear dynamic equilibrium equations is solved at each time increment. The solution is then calculated by using Newton's method. An automatic incrementation scheme provided in ABAQUS was also used in order to control the accuracy of the solution. Artificial damping, called the ALPHA parameter was also introduced in the model. A value of $\alpha = -0.05$ was used because this introduced just enough artificial damping in the system to allow the automatic time stepping procedure to work smoothly.

WARP3D The Newmark time integration scheme within WARP3D was used in order to obtain the dynamic response of the cracked specimen subjected to rapid load. This code utilizes an implicit scheme to integrate through time.

Element formulations accommodate finite-strains using Newmark's method. The code provides three-dimensional, i.e. 8,9,12,15 and 20, node brick elements. Several nonlinear constitutive models are available. The program runs efficiently on workstation environments as well as personal computer.

FE models were analysed using the above software for linear and non-linear material. Finally, the results between ABAQUS and WARP3D were compared.

4.2.3 Analyses Results

Cracked Plate Under Impact Tension

Figures 4.7 and 4.8 compare the J-integral results of cracked plates under impact tension from WARP3D and ABAQUS under elastic and elastic-plastic conditions respectively. In the legend, ABAQUS and WARD3D static equation indicates the J-integral results calculated by using conventional J-integral formulation. Meanwhile WARP3D dynamic equation means that inertia effects were included. The J-integral values were taken from the averaged values between the second and the fourth contours.

Effects of inertia on the J-integral values under elastic conditions can be seen in Figure 4.7. The results show a good agreement between WARP3D and ABAQUS. At the maximum point, the difference is less than 5% between the conventional J-integral formulation and the one with inertia effect. For the elastic-plastic case in Figure 4.8, the results also show good agreement between two programs. The difference at the maximum point is 18%.

Ramp Loading on Cracked Bend Specimen

Figures 4.9 and 4.10 compare the J-integral results of the three point bend fracture toughness specimen under rapid load from WARP3D and ABAQUS under elastic and elastic-plastic conditions respectively. The average J values were taken from

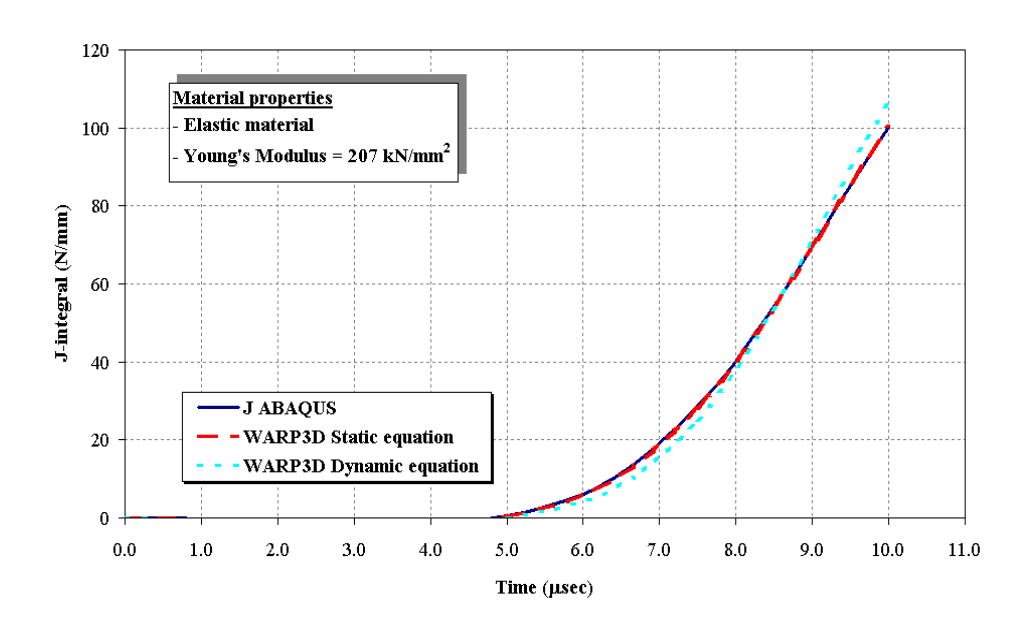


Figure 4.7: Time variation of dynamic J-integral of cracked plate with ramp load applied within 5μ sec. and held constant for 10μ sec. (Elastic condition)

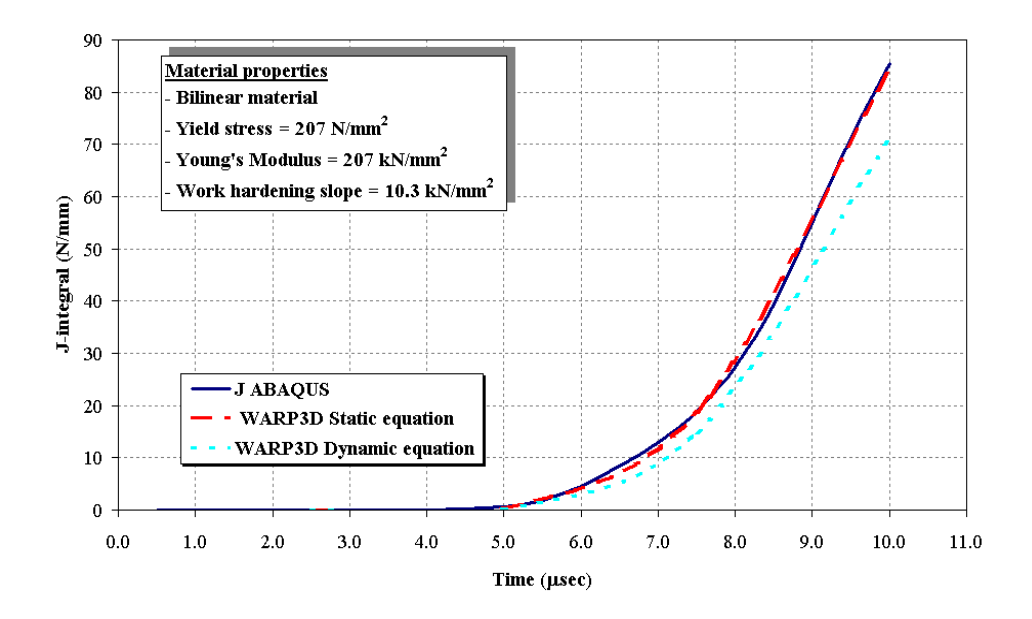


Figure 4.8: Time variation of dynamic J-integral of cracked plate with ramp load applied within 5μ sec. and held constant for 10μ sec. (Elastic-Plastic condition)

contours close to the crack tip (excluding the first contour). Both elastic and elastic-plastic cases, J values obtained from WARP3D showed good agreement with J values from ABAQUS. Therefore it can be concluded that the J-integral results from ABAQUS can be used to calculate J-integral values of cracked specimen under intermediate loading rates and monotonic loading.

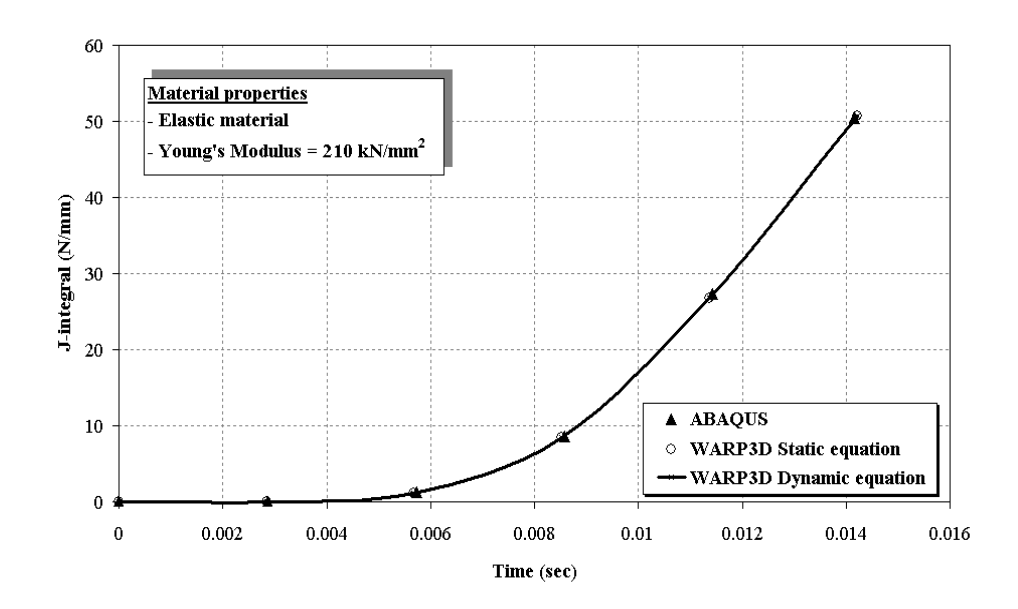


Figure 4.9: Time variation of dynamic J-integral of TPB specimen with ramp load applied within 0.01421 sec. (Elastic condition)

4.3 Effect of Loading Rate on Dynamic Stress Intensity Factor

It is well known that the rate of loading affects the material properties in steel. For structural steels, increasing the loading rate will cause an increase of the yield and tensile strength which basically leads to a reduction of cleavage fracture toughness. In the conventional testing standard, structural integrity is evaluated by fracture toughness tests using pre-cracked specimens. The load is applied statically to the testing specimen. In many dynamic events such as earthquakes, the structural

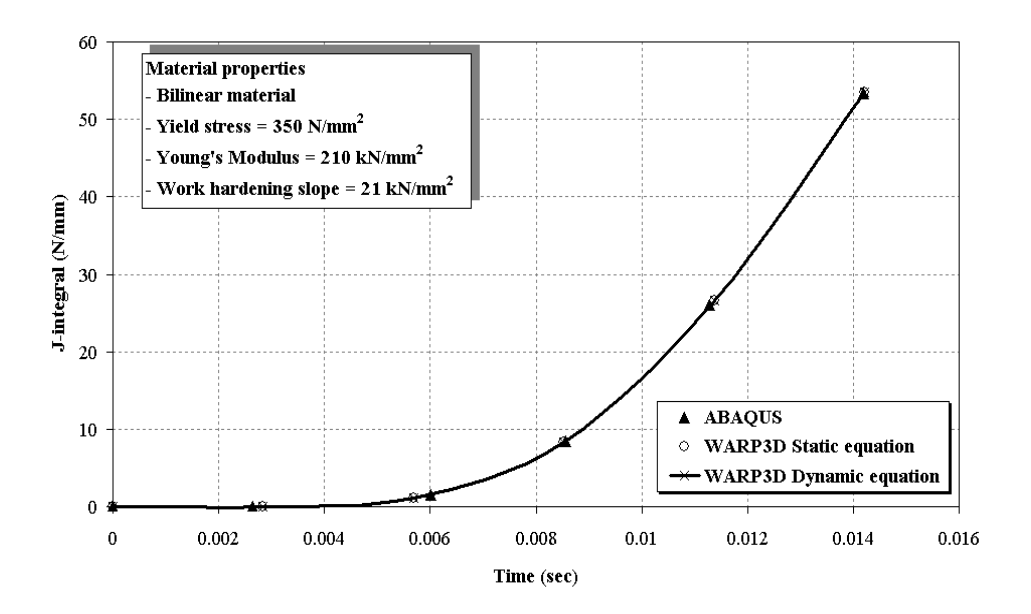


Figure 4.10: Time variation of dynamic J-integral of TPB specimen with ramp load applied within 0.01421 sec. (Elastic-Plastic condition)

member may be subjected to a high rate of loading. The conventional testing method may not be sufficient for such cases. Therefore the rate of loading should be taken into account in testing procedures.

Civil engineering structures, e.g. road and railway bridges, may also be subjected to loading rates that are greater than those prescribed in current fracture toughness testing standards [14]. As mentioned in Chapter 2, the loading rate can be classified into three categories, i.e. slow, intermediate and dynamic. There are many examples of dynamic loading rate effects on the structure. For example, brittle fractures at the steel connections were widely found during the 1994 Northridge and the 1995 Kobe earthquakes. The dynamic loading rate effects which are generated by ground movement fall into the intermediate category.

In this part of the study, the effect of loading rate on the three point bend (TPB) fracture toughness specimen of steel subjected to rapid ramp loading is explored. A series of loading rates is applied to the TPB specimen. Two types of loading are considered, i.e. applied linearly until a given time and stopped/released, or applied

linearly until a given time and maintained at constant load. The linear elastic and elastic-plastic material effects are also investigated.

4.3.1 TPB Specimen Under Rapid Loading

This study was mainly focused on the behaviour of the TPB specimen under impact loading. Referring to Chapter 2, earthquake ground motion produced dynamic loading rate effects in the intermediate loading rate range. Therefore, the ranges of applied loading in this study will focus only in this range. The geometry of the TPB specimen was chosen from BS6729 [6]. In order to get the full response of the TPB specimen, two-dimensional plane strain finite element analysis was performed on the full specimen. The TPB specimen has dimensions 200 mm long x 50 mm width x 25 mm thick. As shown by the results from section 5.2, the J-integral evaluation from the ABAQUS finite element program has proved to give a sufficiently accurate answer for static up to intermediate loading rates. Therefore, the ABAQUS finite element program was used for all of this part of the study.

Studies were conducted on a 2-dimensional specimen for the following cases:

- case a) TPB under 1417.1 $\rm N \cdot mm^{-1.5} \cdot s^{-1}$ applied loading rate.
- case b) TPB under 2836.9 $\rm N \cdot mm^{-1.5} \cdot s^{-1}$ applied loading rate.
- case c) TPB under 9736.8 $\textrm{N}\cdot\textrm{mm}^{-1.5}\cdot\textrm{s}^{-1}$ applied loading rate.
- case d) TPB under 14215.3 $\rm N \cdot mm^{-1.5} \cdot s^{-1}$ applied loading rate.
- case e) TPB under 17195.2 $\textrm{N}\cdot\textrm{mm}^{-1.5}\cdot\textrm{s}^{-1}$ applied loading rate.
- case f) TPB under 26895.4 $\rm N{\cdot}mm^{-1.5}{\cdot}s^{-1}$ applied loading rate.
- case g) TPB under 30240.3 N·mm $^{-1.5}$ ·s $^{-1}$ applied loading rate.

Finite Element Analyses

As in the analyses of the ramp loading on the TPB specimen, a multi step submodelling technique was adopted. The pre-processing package PATRAN V9.0 [15] was used to generate the input data for analysing in the ABAQUS FE program. The finite element analyses used 2D isoparametric elements (i.e. element type CPE8R in ABAQUS). There were two layers of the mesh around the crack tip. At a small region close to the crack tip, a fine mesh was modelled to ensure accuracy of the results. At the crack tip, the typical blunt-tip model was employed in both elastic and elastic-plastic analyses in order to avoid the difficulties in getting converged solutions. The initial root radius was assumed to be 0.03 mm. Twenty contours were modelled for extracting the J-integral values. The finite element model is shown in Figure 4.11.

Both elastic and elastic-plastic material properties were used in this study. The elastic material had a Young's modulus of $210 \ kN/mm^2$. Bi-linear material properties were assumed for the elastic-plastic analyses with a yield stress of $350 \ N/mm^2$. Strain hardening was assumed to be isotropic with a slope of 21 GPa. The conventional engineering strain, ε_E and engineering (nominal) stress, σ_E values were converted to true strain and true stress by using Equation (4.3) and Equation (4.4). After that the true stress and true strain values were inserted into the input file.

The applied loading was assumed linear up to a maximum load 20 kN. There were two types of loading as follow:

- 1. Applied load up to a maximum load.
- 2. Applied load up to a maximum load and held constant for a certain time.

During the applied loading, the load-time history was plotted in order to check the rate of loading on the specimen. The calculation of loading rate was based on BS6729. For the response of specimen focused on the maximum load, the rate of

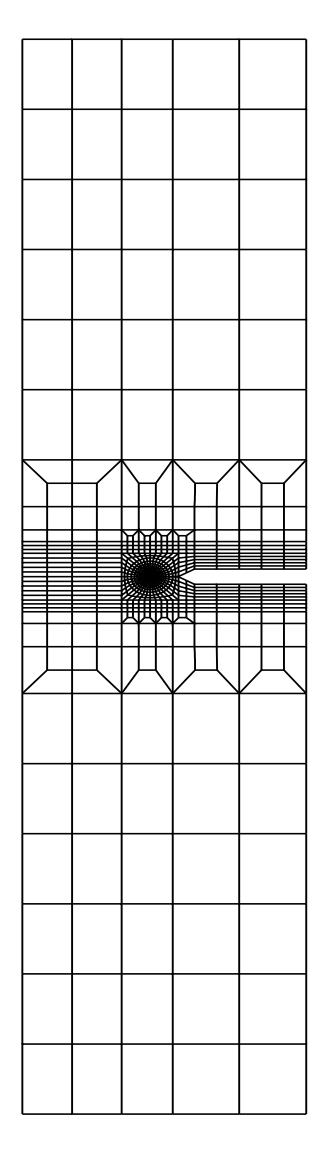




Figure 4.11: Finite element model of full TPB specimen

applied loading was obtained from the equation below:

$$\dot{K}_I = \left(\frac{\dot{P}S}{BW^{1.5}}\right) Y_1 \tag{4.5}$$

where \dot{K}_I is the rate of change of stress intensity factor with time, \dot{P} is the rate of change of force with time, S is the distance between outer loading points of the test piece, B is the specimen thickness, W is the effective test piece width, Y_1 is the stress intensity coefficient for bend test pieces, taken as 3.14 for this specimen.

The results of J-integral from ABAQUS were compared with an estimation method. The estimation method was based on a linear relationship between J and the geometrically normalised deformation energy U given by ESIS-P2 (1992) [16] as shown below:

$$J = \eta \frac{U}{B_n(W - a_0)} \tag{4.6}$$

where U is area under load versus load-line displacement curve, B_n is the specimen thickness, W is the specimen width and a_0 is initial length of the crack. The value of the proportionality factor η depends on type of specimen. For a TPB specimen, the standard ESIS-P2 suggests a value of $\eta = 2$.

The two-dimensional plane-strain model was used for this study. The implicit integration technique, called Hilber-Huges-Taylor (HHT) operator, provided in ABAQUS/Standard was used to calculate the response of the TPB specimen. The dynamic equilibrium equation used in the finite element method given by:

$$M\ddot{u}_{n+1} + (1+\alpha)(I_{n+1} - P_{n+1}) - \alpha(I_n - P_n) = 0$$
(4.7)

where M is the consistent mass matrix, n is the current time step and superscript dots denote time derivatives. The internal force vector I is obtained from the finite element stiffness and the displacements. The displacement vector u and velocity vector \dot{u} are defined using the Newmark family scheme:

$$\{u_{n+1}\} = \{u_n\} + \Delta t\{\dot{u}_n\} + \frac{\Delta t^2}{2}(1 - 2\beta)\{\ddot{u}_n\} + \Delta t^2\beta\{\ddot{u}_{n+1}\}$$
(4.8)

$$\{\dot{u}_{n+1}\} = \{\dot{u}_n\} + \Delta t(1-\gamma)\{\ddot{u}_n\} + \gamma\{\ddot{u}_{n+1}\}$$
(4.9)

where $\beta = (1-\alpha)^2/4$, $\gamma = 1/2$ - α and -1/3 $\leq \alpha \leq 0$. The above equations represent a set of non-linear algebraic equations that are solved using Newton's method. The advantage of the HHT operator is that the numerical damping is controlled independently of the time increment by the parameter α . An α of -0.05 was used in the analyses which provided for a small amount of damping and is the recommended value by ABAQUS.

Analysis Results

Figures 4.12 to 4.18 compare the results of J-integral between elastic and elastic-plastic conditions under different loading rates and represent the results from case 1a to case 1g respectively. The results of these analyses showed a significant effect of loading rate. Immediately load is applied, the specimen starts to vibrate effectively at its natural frequency. From Figures 4.12 to 4.18, the results showed that increasing loading rates increased the amplitude of vibration. In contrast, the J-integral values decreased. Comparison between elastic and elastic-plastic cases, the J-integral values from elastic-plastic case were higher than elastic case in all cases.

Figures 4.19 to 4.25 compare the results of J-integral between elastic and elasticplastic conditions under different loading rate and represent the results from case 2a to case 2g respectively. Increasing the loading rate causes an oscillation about the maximum load when the load is maintained constant. For example, the peak value of J is increased by about 13% for a rate of loading corresponding to a \dot{K}

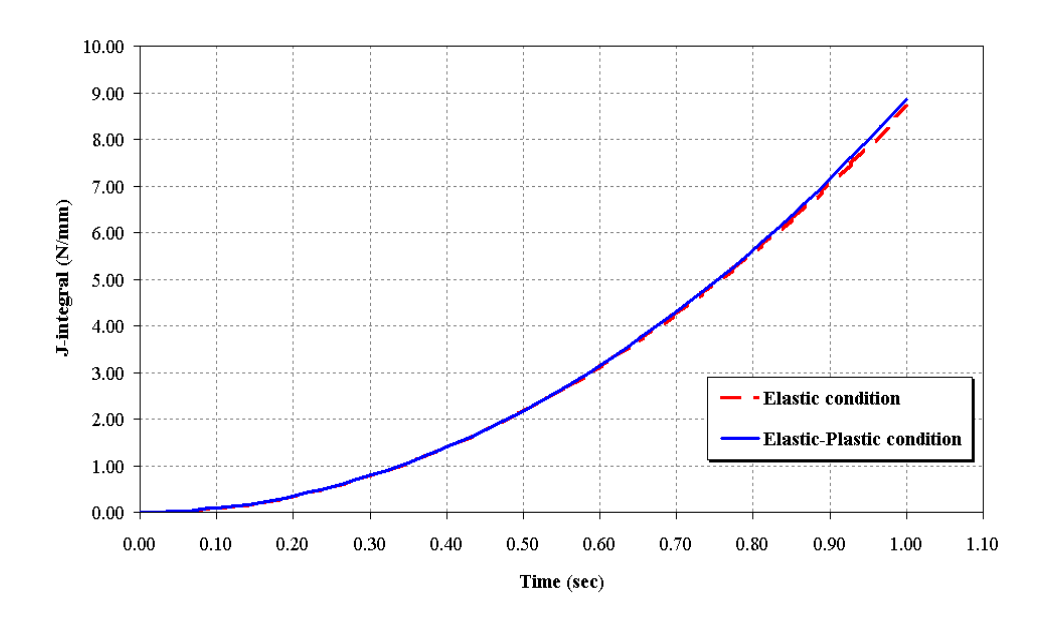


Figure 4.12: Time variation of dynamic J-integral of TPB specimen with ramp load applied within $1.0~{\rm sec.}$

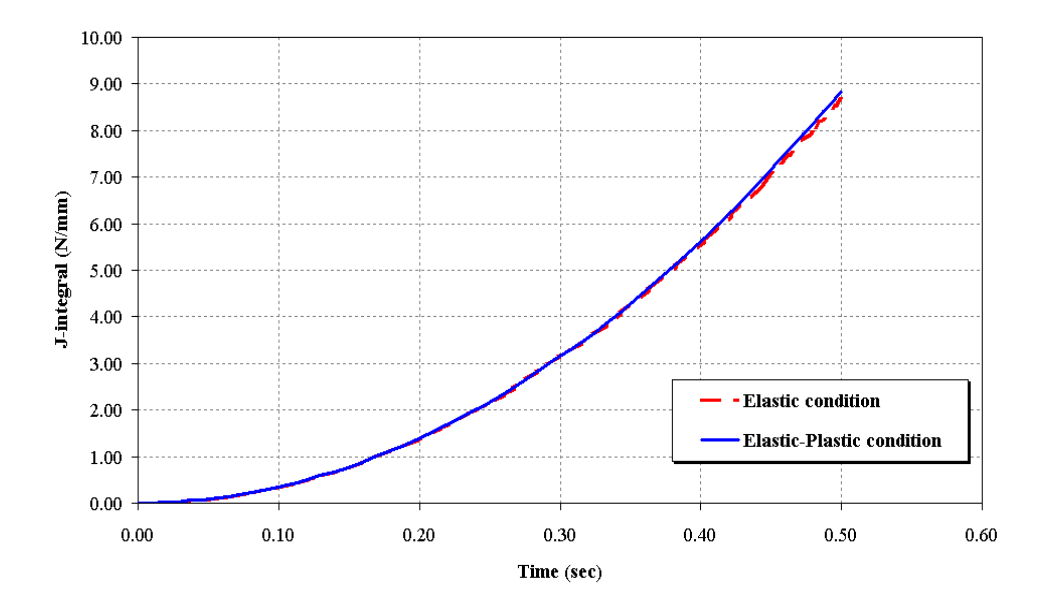


Figure 4.13: Time variation of dynamic J-integral of TPB specimen with ramp load applied within $0.50~{\rm sec.}$

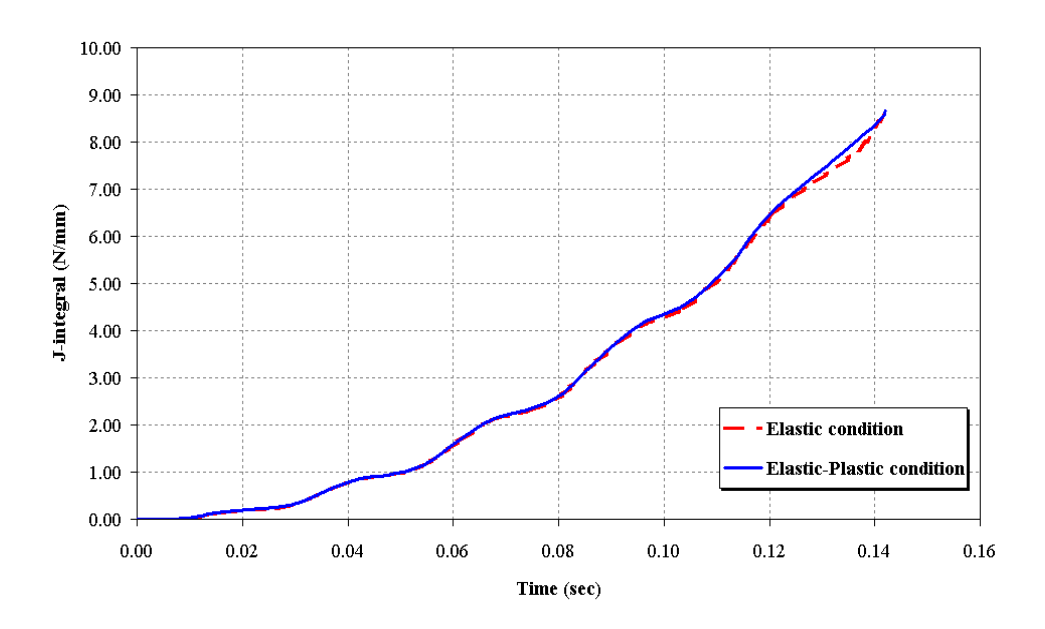


Figure 4.14: Time variation of dynamic J-integral of TPB specimen with ramp load applied within $0.1421~{\rm sec.}$

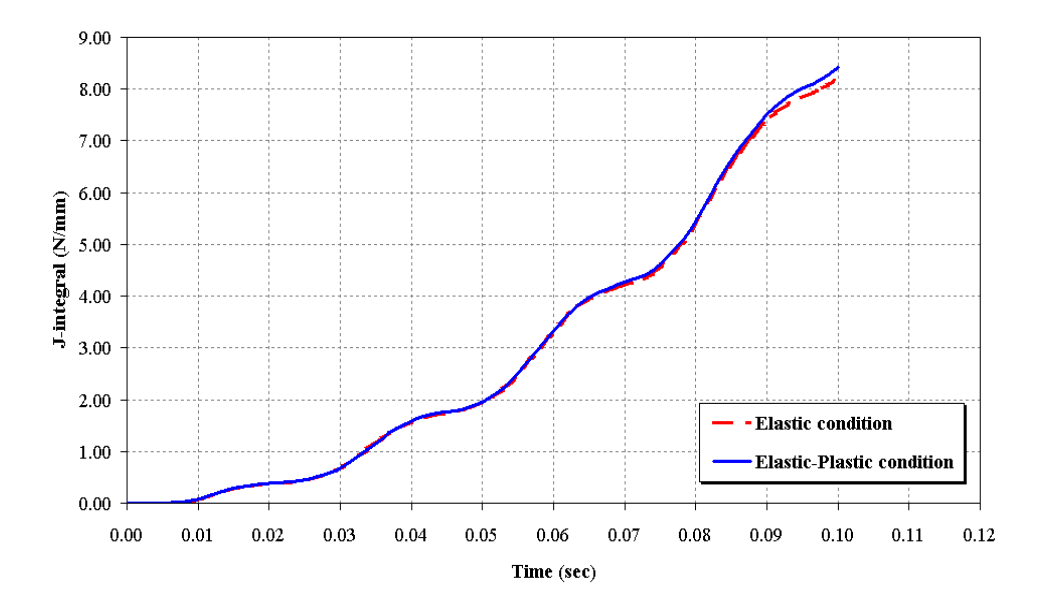


Figure 4.15: Time variation of dynamic J-integral of TPB specimen with ramp load applied within $0.10~{\rm sec.}$

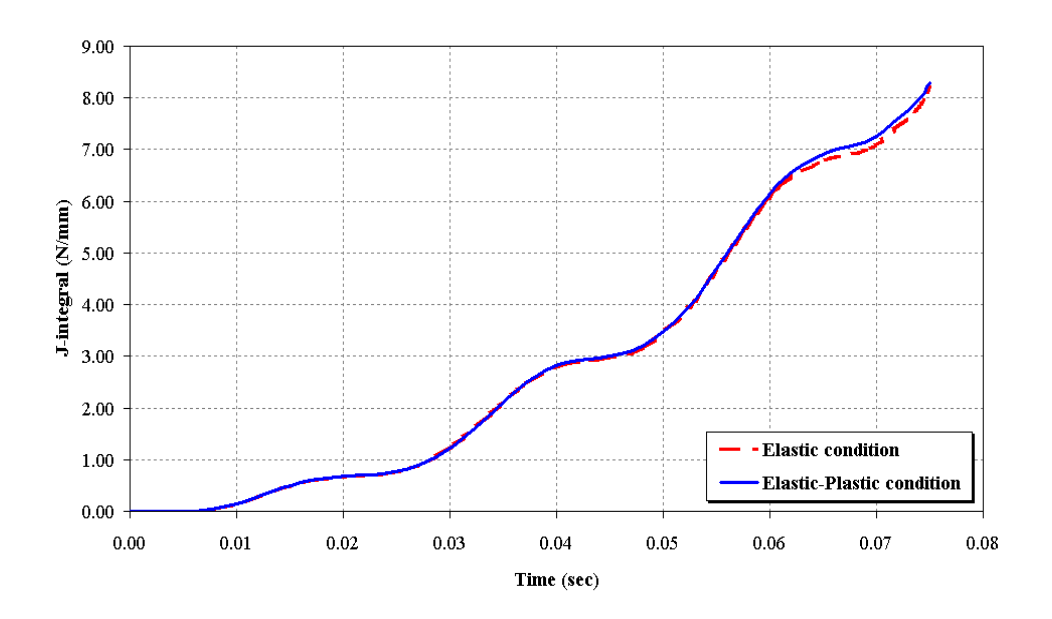


Figure 4.16: Time variation of dynamic J-integral of TPB specimen with ramp load applied within $0.075~{\rm sec.}$

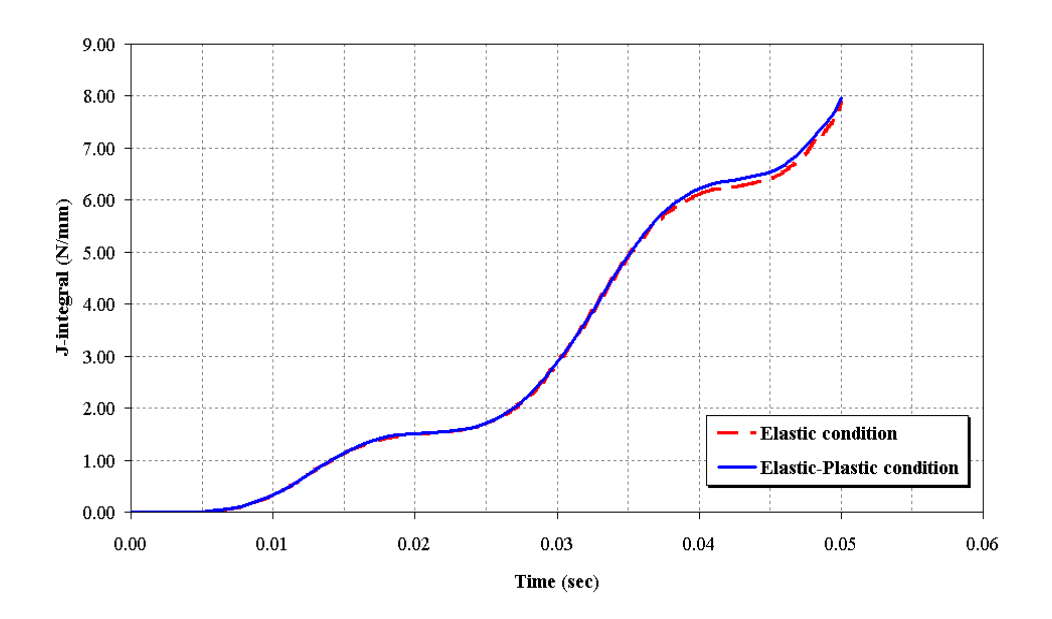


Figure 4.17: Time variation of dynamic J-integral of TPB specimen with ramp load applied within $0.05~{\rm sec.}$

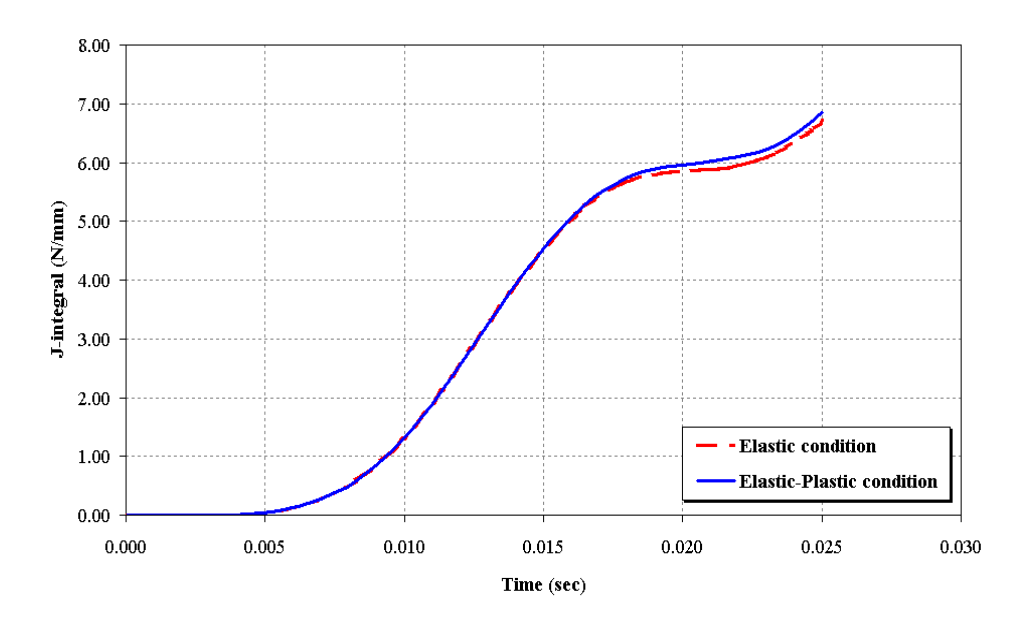


Figure 4.18: Time variation of dynamic J-integral of TPB specimen with ramp load applied within 0.025 sec.

of 17195.2 N·mm^{-1.5}·s⁻¹ and by about 30 % for a rate of loading giving a \dot{K} of 30240.3 N·mm^{-1.5}·s⁻¹ The magnitude of vibration depends on the rate of loading relative to the natural frequency of specimen. The elastic-plastic case also gives higher J-integral values than elastic case. It can be seen that J-integral results involve partial unloading. Even though the formal definition of J is violated when unloading occurs, calculating J by assuming high hardening material can provide a fairly good result. When low hardening material was assumed, the results appear to show path dependence in the J-integral results. Therefore, the validity of J-integral results under elastic-plastic conditions depends on the assumed material properties.

Figures 4.26 and 4.27 show the variation of J-integral values under different loading rates. It can be seen that increasing the loading rate decreases the J-integral values in both elastic and elastic-plastic cases. The estimation values of J-integral also give a good agreement with the results from finite element analysis.

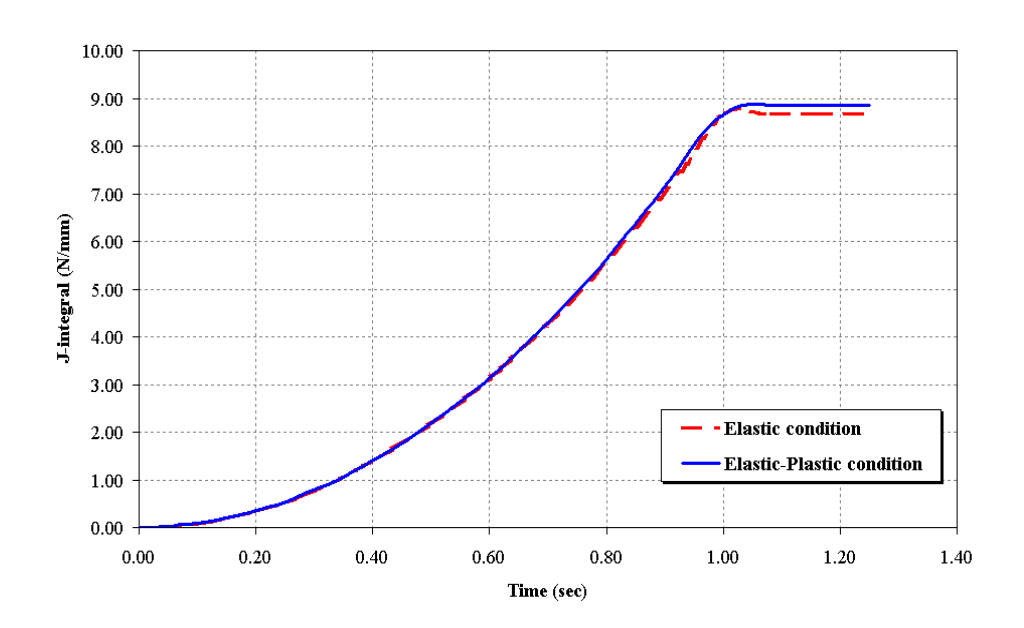


Figure 4.19: Time variation of dynamic J-integral of cracked plate with ramp load applied within 1.0 sec. and held constant for 1.25 sec.

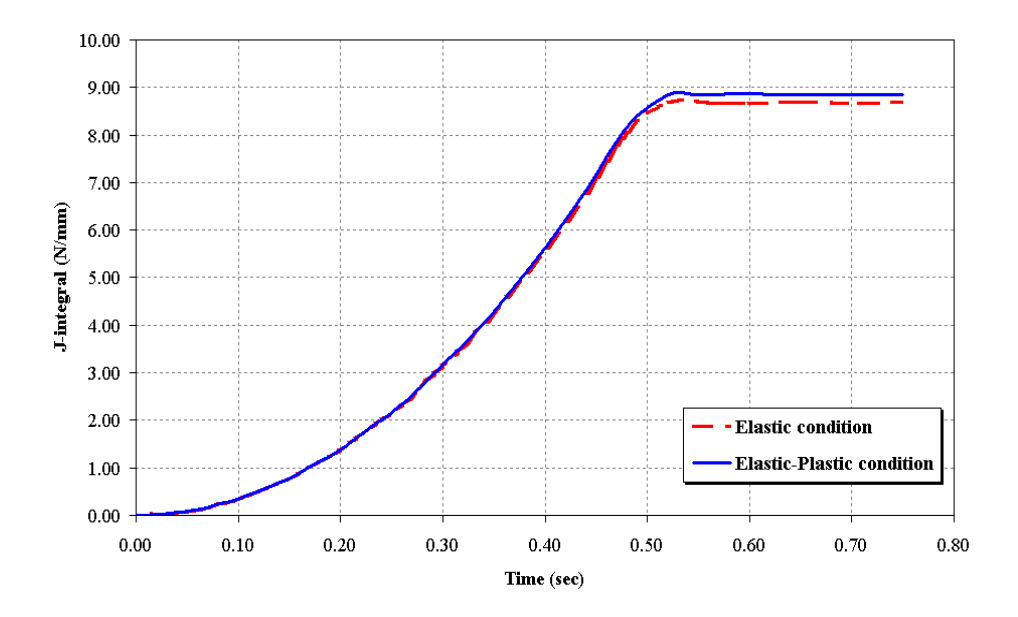


Figure 4.20: Time variation of dynamic J-integral of cracked plate with ramp load applied within 0.50 sec. and held constant for 0.75 sec.

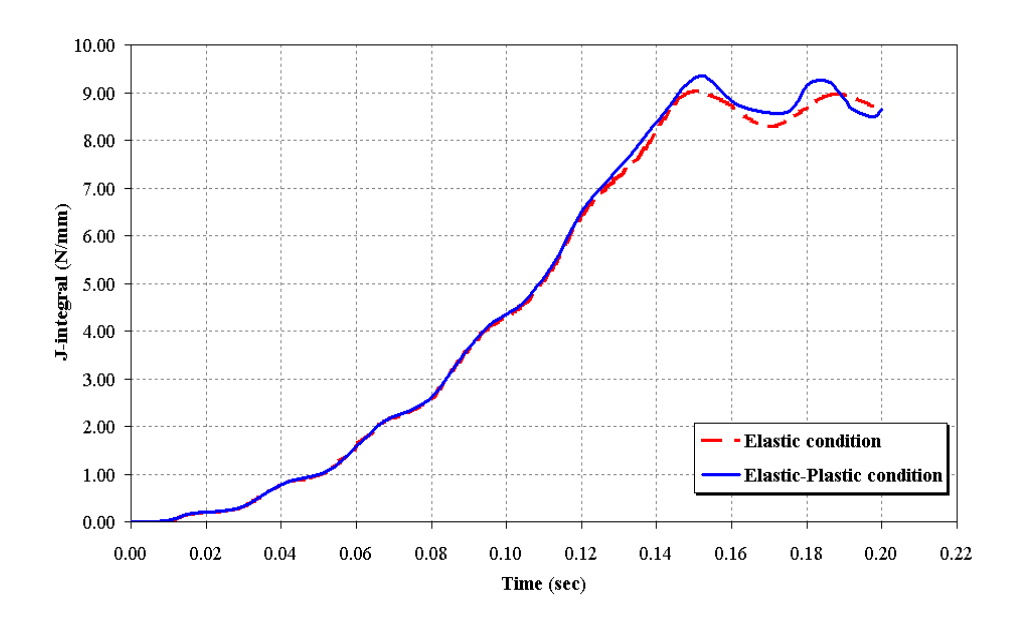


Figure 4.21: Time variation of dynamic J-integral of cracked plate with ramp load applied within 0.1421 sec. and held constant for 0.20 sec.

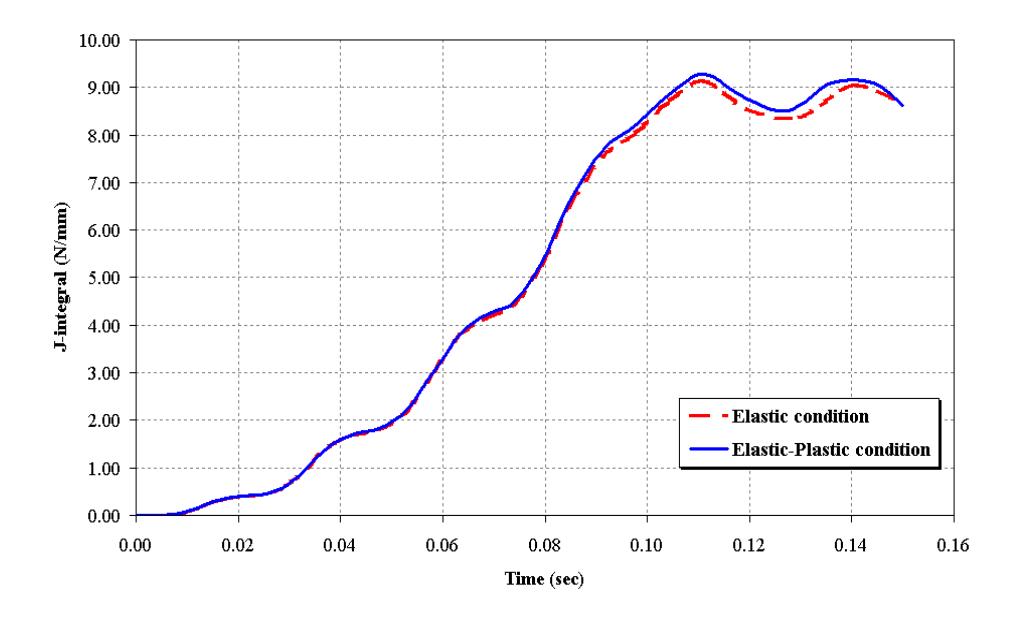


Figure 4.22: Time variation of dynamic J-integral of cracked plate with ramp load applied within 0.10 sec. and held constant for 0.15 sec.

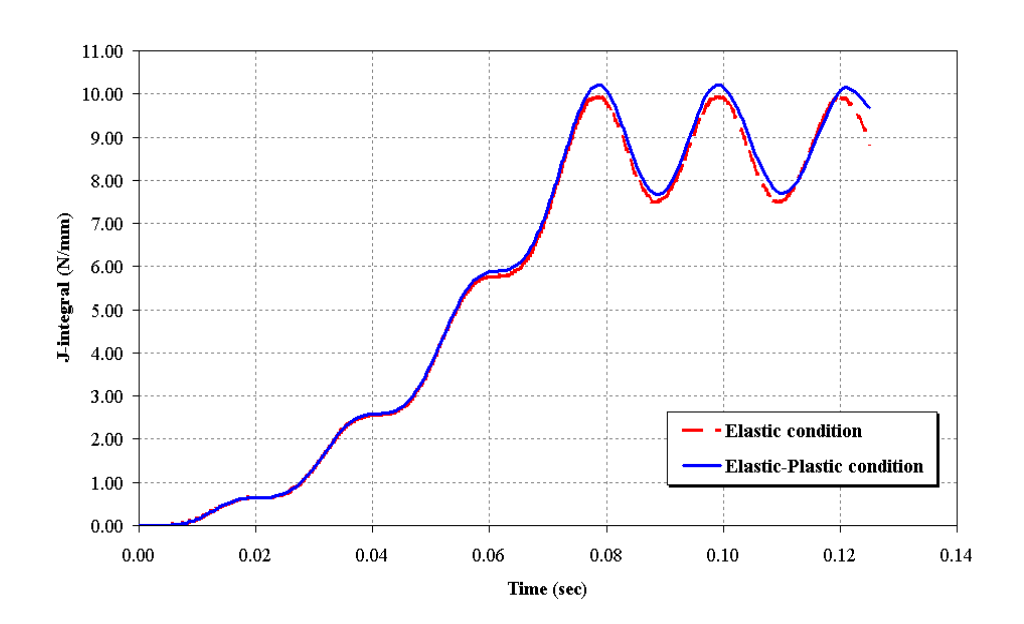


Figure 4.23: Time variation of dynamic J-integral of cracked plate with ramp load applied within 0.075 sec. and held constant for 0.125 sec.

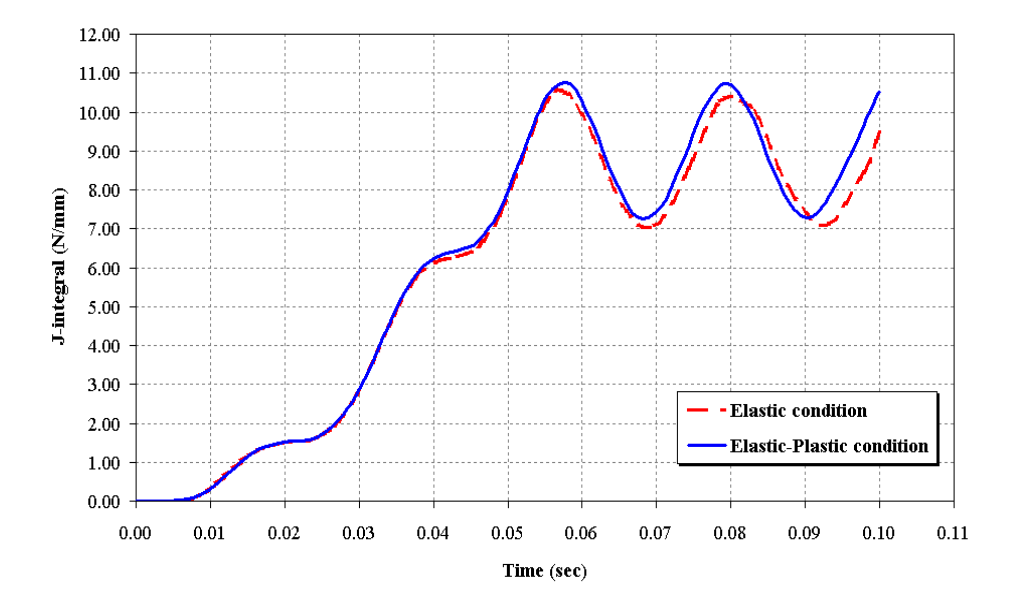


Figure 4.24: Time variation of dynamic J-integral of cracked plate with ramp load applied within 0.05 sec. and held constant for 0.10 sec.

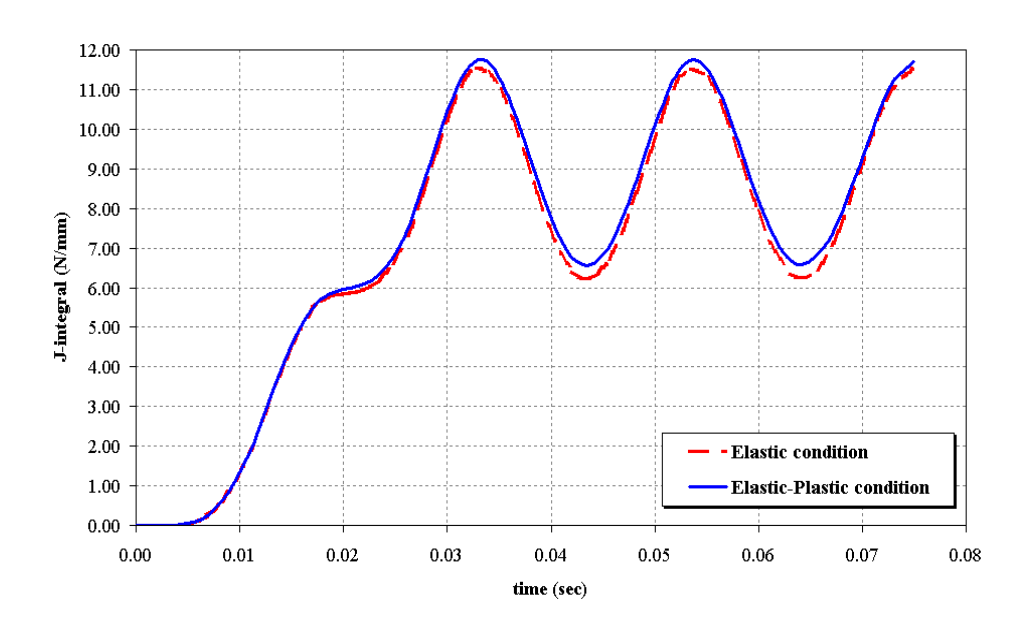


Figure 4.25: Time variation of dynamic J-integral of cracked plate with ramp load applied within 0.025 sec. and held constant for 0.075 sec.

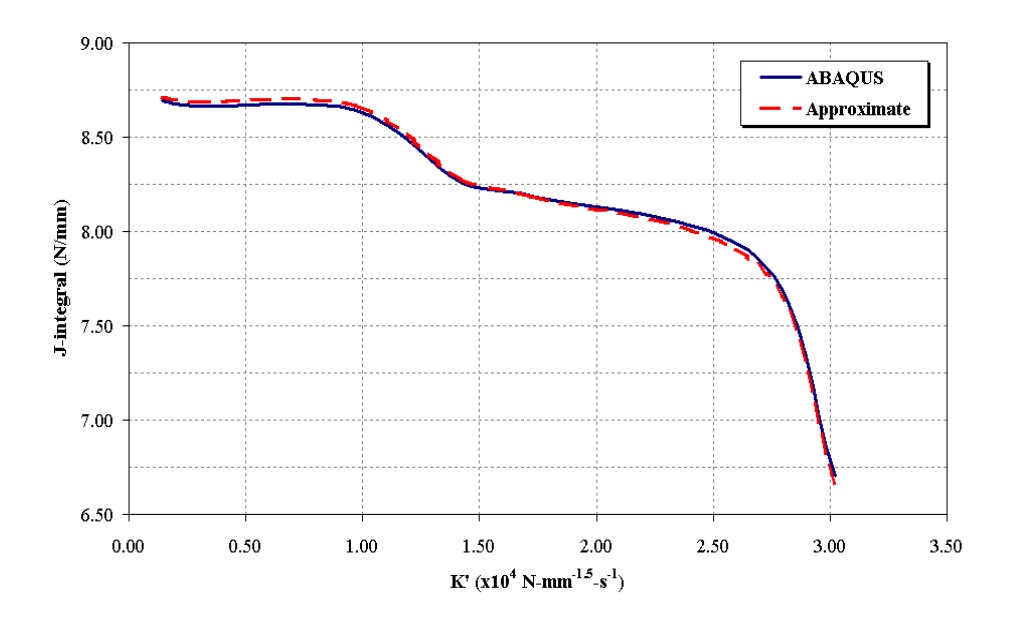


Figure 4.26: Comparison of J-integral values between ABAQUS and approximate method at different loading rate (Elastic condition)

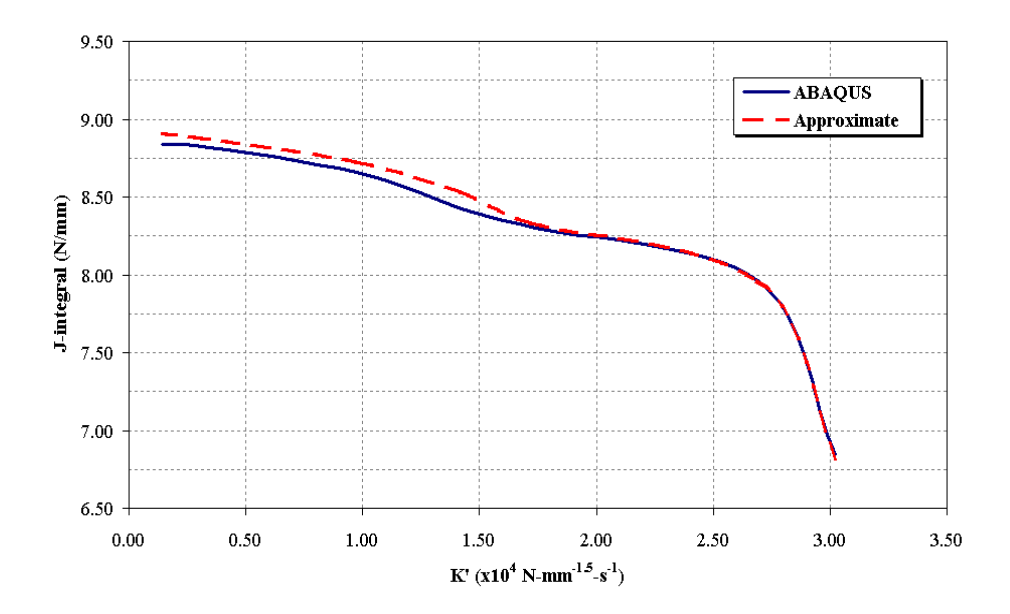


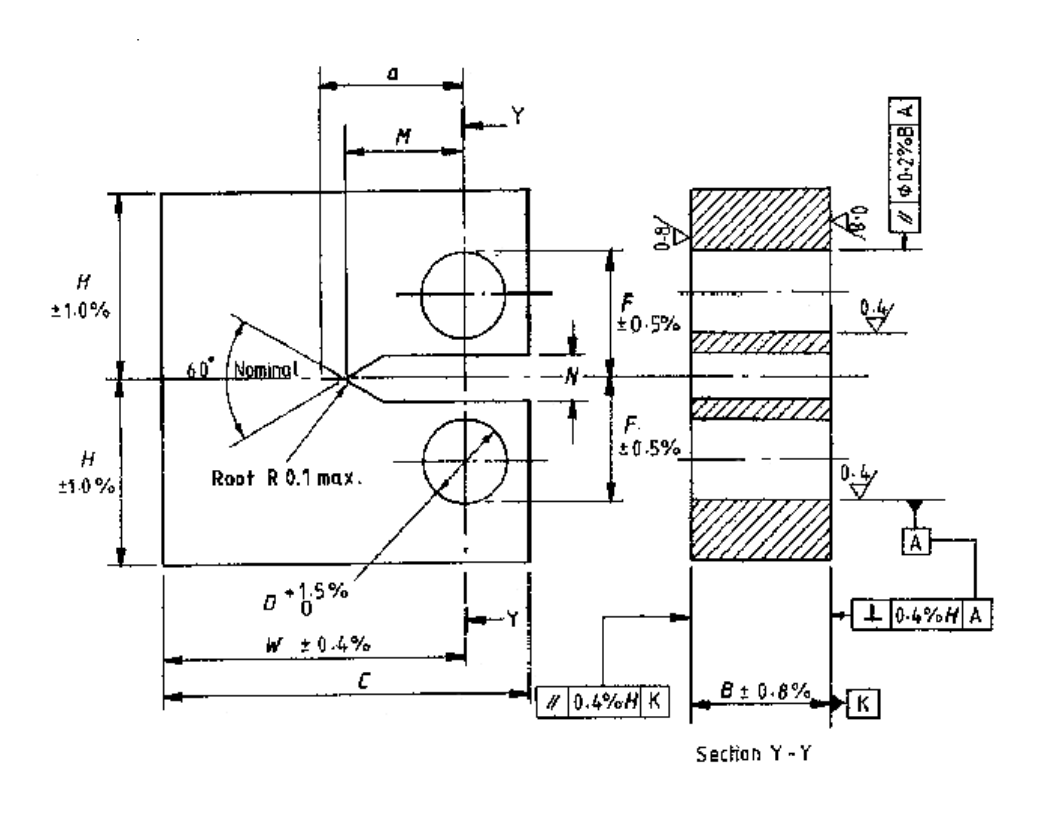
Figure 4.27: Comparison of J-integral values between ABAQUS and approximate method at different loading rate (Elastic-Plastic condition)

4.3.2 Compact Tension (CT) Specimen Under Cyclic Loading

This section is a study of a cracked specimen under dynamic loading focused on the effect of cyclic loading. The cracked specimen considered is a compact tension specimen. The geometry of the compact tension (CT) specimen was chosen from BS6729 [6] as shown in Figure 4.28 with dimensions 30 mm crack length x 25 mm thick x 50 mm width. Finite element analyses were conducted on a two-dimensional plane-sided CT specimen using the ABAQUS FE package. Only half of the CT specimen was modelled by taking advantage of symmetry.

Finite Element Analyses

The pre-processing package PATRAN V9.0 [15] was used to generate the input data for analysing in the ABAQUS FE program. The finite element analyses used 2D isoparametric elements (i.e. element type CPE8R in ABAQUS). At a small



W is the effective test piece width

Total width C = 1.26 W min.

Thickness B = 0.5 W

Holf height H = 0.6 W

Hole diameter D = 0.25 W

Half distance between hole outer edges F = 1.8 D = 0.065 W max.

Effective notch length M = 0.26 W to 0.40 W

Effective erack length e = 0.45 W to 0.55 W

All dimensions are in millimatres.

Figure 4.28: Proportional dimensions and tolerances for test CT specimen [6]

region close to the crack tip, a fine mesh was modelled to ensure accuracy of the results. At the crack tip, the typical blunt-tip model was employed in both elastic and elastic-plastic analyses in order to avoid the difficulties in getting converged solutions. The initial root radius was assumed to be 0.019 mm. Eighteen contours were modelled for extracting the J-integral values. At the pin hole, linear elastic elements were used to fill in the hole. The loads were then applied at the centre of the hole. The finite element model is shown in Figure 4.29.

Elastic and elastic-plastic material properties were again used in this study. The elastic material had a Young's modulus of $210~kN/mm^2$. Two bi-linear material properties were considered for the elastic-plastic analyses, i.e. a yield stress of $350~N/mm^2$ with 21 GPa strain hardening and a yield stress of $350~N/mm^2$ with $550~N/mm^2$ ultimate strength at 15% strain.

The rate of loading was calculated by using the plot of load-time history during the rising load step. The calculation of loading rate was based on BS6729 as shown below:

$$\dot{K}_I = \left(\frac{\dot{P}Y_2}{BW^{0.5}}\right) \tag{4.10}$$

where \dot{K}_I is the rate of change of stress intensity factor with time, \dot{P} is the rate of change of force with time, Y_2 is the stress intensity coefficient for bend test pieces, taken as 13.65 for this specimen, B is the specimen thickness, W is the effective test piece width.

Hence, studies were conducted for the following cases:

case a) CT under static condition.

case b) CT under 2244 $\text{N} \cdot \text{mm}^{-1.5} \cdot \text{s}^{-1}$ applied loading rate.

case c) CT under 14942 $\text{N}\cdot\text{mm}^{-1.5}\cdot\text{s}^{-1}$ applied loading rate.

case d) CT under 22395 $\text{N} \cdot \text{mm}^{-1.5} \cdot \text{s}^{-1}$ applied loading rate.

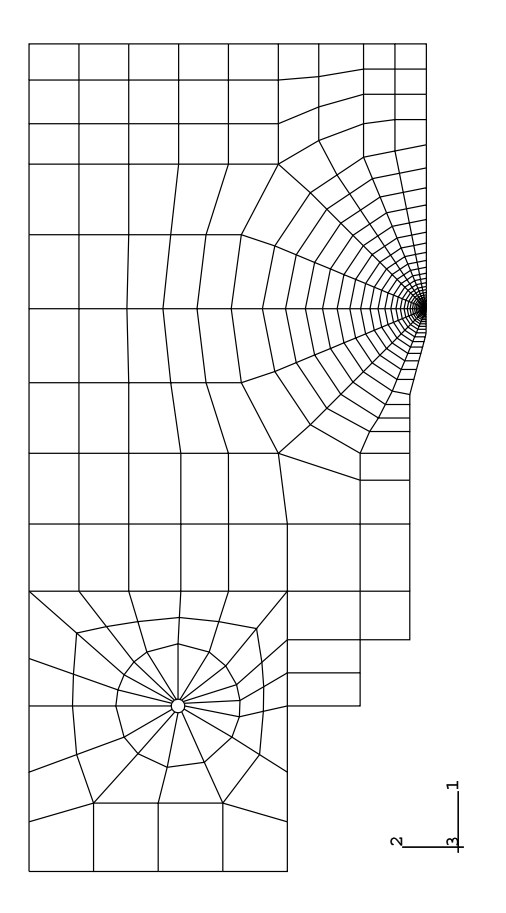


Figure 4.29: Finite element model of CT specimen

The analyses were conducted under displacement control at a constant loading rate. The loading rate was calculated from the rising part of the first cycle. Applied cyclic loading with a stress ratio equal to zero was used throughout this study. As mentioned earlier, there was a 0.019 mm initial blunt at the crack tip. Hence, the original crack face is 0.019 mm above the symmetry plane. In order to avoid the contact of the crack faces which may occur during analyses, the maximum applied displacement was carefully checked before further analysis of the model. Two maximum applied displacements at the loading points, i.e. 0.1 and 0.35 mm, which provided the maximum applied load within the elastic and elastic-plastic range respectively were investigated in this study.

Since the conventional J-integral based on deformation theory is undefined when unloading occurs, an engineering approximation had to be made in order to assess the cyclic effect on J-integral. Landes and McCabe [23] introduced an approximate method using an upper envelope of the load-displacement record to calculate J. The area under the load-displacement curve was then used to calculate J by using equation 4.6. The value of the proportionality factor η for the CT specimen was calculated by the following equation:

$$\eta = 2 + 0.522 \frac{b_0}{W} \tag{4.11}$$

where η is a dimensionless constant, W is the specimen width and b_0 is the initial ligament length.

For the case of applied displacements within the elastic-plastic range, the CTOD value was also obtained from displacements of nodes defining the crack flank using the 45° intercept procedure. If the intercept fell between two nodes, displacements of the nearest nodes were interpolated. The CTOD value was then converted to a J-integral value by using the relationship between J-integral and CTOD from the

following equation:

$$J = m\sigma_{flow}\delta \tag{4.12}$$

where m is the proportionality factory, i.e. $1 \le m \le 2$, taken as 1.7 in this study. δ is the CTOD and σ_{flow} is the flow stress (typically the average of ultimate and yield strengths).

Finally, the results of J-integral from the approximation method were then compared with those obtained from ABAQUS.

Analysis Results

For the case of applied loading within the elastic range, the results of J-integral are shown in Tables 4.1 and 4.2 for elastic and elastic-plastic materials respectively. Table 4.1 shows the results of J-integral obtained from ABAQUS and approximation method under elastic conditions for different loading rates. Five integration contours were selected for these J-integral calculations. The results of J-integral for each set of contours show good path independence. Both methods give a close agreement with the maximum error 5.71%. At increasing loading rates of cyclic load, there is no significant effect on the J-integral results.

Table 4.1: Comparison of J-integral results under applied 0.1 mm displacement (elastic case)

Loading rate	ABAQUS	Approximate	Error
$(\text{N} \cdot \text{mm}^{-1.5} \cdot \text{s}^{-1})$	(N/mm)	(N/mm)	(%)
Static	7.223	6.946	3.99
2244.4	5.573	5.272	5.71
14942.3	5.553	5.258	5.61
22395.7	5.540	5.260	5.32

Table 4.2 shows the results of J-integral obtained from ABAQUS and approximation method for the elastic-plastic material but at low loads. The results also

Table 4.2: Comparison of J-integral results under applied 0.1 mm displacement (elastic-plastic case)

Loading rate	ABAQUS	Approximate	Error
$(N \cdot mm^{-1.5} \cdot s^{-1})$	(N/mm)	(N/mm)	(%)
Static	7.244	6.874	5.38
2244.4	5.550	5.245	5.82
14942.3	5.531	5.243	5.49
22395.7	5.517	5.246	5.17

give a close agreement between ABAQUS and the approximation method with maximum error 5.82%. As mentioned earlier, the conventional J-integral based on deformation plasticity theory is undefined when unloading occurs. The J-integral results from ABAQUS shown in this study are valid when a very high hardening material is assumed. If low hardening material is assumed, the results appeared to be path dependent. The J-integral results from ABAQUS are valid only for the rising part of the first cycle. For the J-integral obtained from approximation method, the results obtained from the upper envelope of the load-displacement record can provide a tool in the determination of cyclic effects on J-integral value.

For the case of applied loading in the elastic-plastic range, the results of J-integral are shown in Table 4.3. In Table 4.3, $J_{Approximate}$ and J_{CTOD} have been calculated using equations 4.6 and 4.12 respectively while J_{ABAQUS} was obtained directly from ABAQUS. Again the results of J-integral obtained from ABAQUS are also valid only the rising load of the first cycle. It can be seen that the results of J-integral obtained from the different approaches give a close agreement. It must be emphasized that the results of J_{CTOD} depend highly on stress state and material properties. Increasing the frequency of applied cyclic load has no significant effect on J-integral results.

Table 4.3: Comparison of J-integral results under applied 0.35 mm displacement (elastic-plastic case)

Loading rate $(N \cdot mm^{-1.5} \cdot s^{-1})$	J_{ABAQUS} (N/mm)	$J_{Approximate} \ (N/mm)$	J_{CTOD} (N/mm)
Static	72.14	70.06	74.59
2244.4	57.52	56.38	58.14
14942.3	57.50	56.42	58.14
22395.7	57.52	56.64	58.60

4.4 Closing Remarks

From this study, the J-integral assumption given by Rice [32] has been shown to be sufficient for calculating J-integral under intermediate loading rates. The results from ABAQUS give a good agreement with the results from WARP3D. The effect of loading rate on J-integral can be summarised as follows:

- When the loading rates increase, the applied J-integral decreases for both elastic and elastic-plastic case.
- Rapid load rates cause the specimen to vibrate effectively at its natural frequency.
- The magnitude of oscillation of the specimen depends on the rate of loading relative to the natural frequency.
- The validity of J-integral results under elastic-plastic case when partial unloading occurs depends on the assumed material properties.

The present work has also demonstrated that the estimation method following the European Structural Integrity Society (ESIS) gives a good agreement with the results from finite element analysis.

In the case of CT specimen under cyclic loading condition, the results of Jintegral obtained from CTOD show a good agreement with the estimation method given by ESIS. The effect of loading rates appear to have no significant effects under cyclic loading condition. Therefore, the CTOD approach will be used in next chapter in order to assess the crack tip severity of the cracked connections.

Chapter 5

Submodel Analysis of through-wall crack in minimum structures

In this chapter, finite element technique is used to study the local behaviour of connections with defects within the complete brace caisson. The finite element model of brace caisson (with spring support, Figure 5.1) from the previous section is used in this study. Referring to the results of dynamic response of the brace caisson, it could be seen that the most severe case of the response were 16.4 m wave height (Figure 3.6 and 6.35 sec wave period (Figure 3.5). Therefore those wave conditions will be used in the submodel analysis.

Based on the information, i.e. mode shape of vibration (Figure 5.2) and stress results from dynamic response analyses, the possible location of high stress can occur in connection at the height around 7.175 m above S.W.L. Hence, the 3D-submodel of tubular connection containing assumed through-wall crack will be modeled at this height.



Figure 5.1: Finite element model of brace caisson with spring support

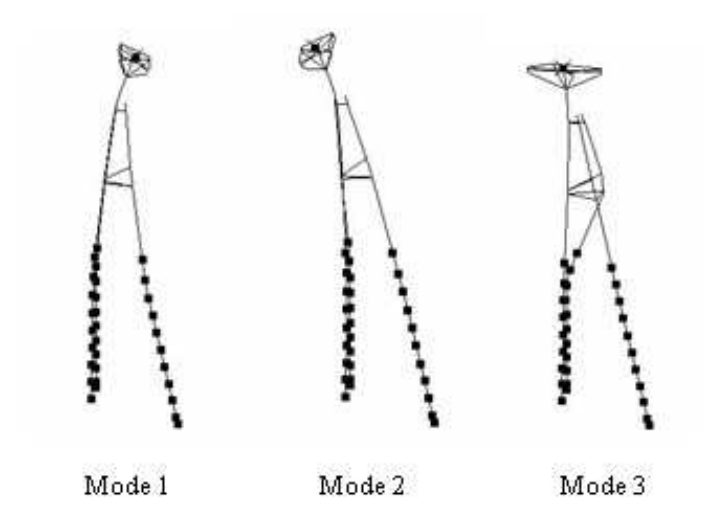


Figure 5.2: Mode shape of vibration for base case at S.W.L.

5.1 Description of 3D-submodel

For the sub models of the connections, three-dimensional shell elements incorporating initial cracks were used. Although the sub model with 3D shell element within the full 3D beam element model proved to be too computationally expensive, it provided valuable understanding of the local behaviour of connections situated in the complete brace caisson. The elements used for the modelling of sub models were the gerneral-purpose three dimensional shell elements, i.e. S4R available in ABAQUS. These elements have six degrees of freedom per node. With an adequately fine mesh, these elements are capable of providing accurate solutions even in complex structures. For the crack tip region, an absolute sharp crack tip should not be adopted in large strain analysis beacause it may cause stress singularity. Therefore a crack tip with initial root radius was introduced in this modelling. The initial root radius was assumed to be 0.03 mm in all cases of study in order to prevent the overlap between the crack faces. Figures 5.3-5.5 shows 3D-submodel and the typical crack tip used in this study.

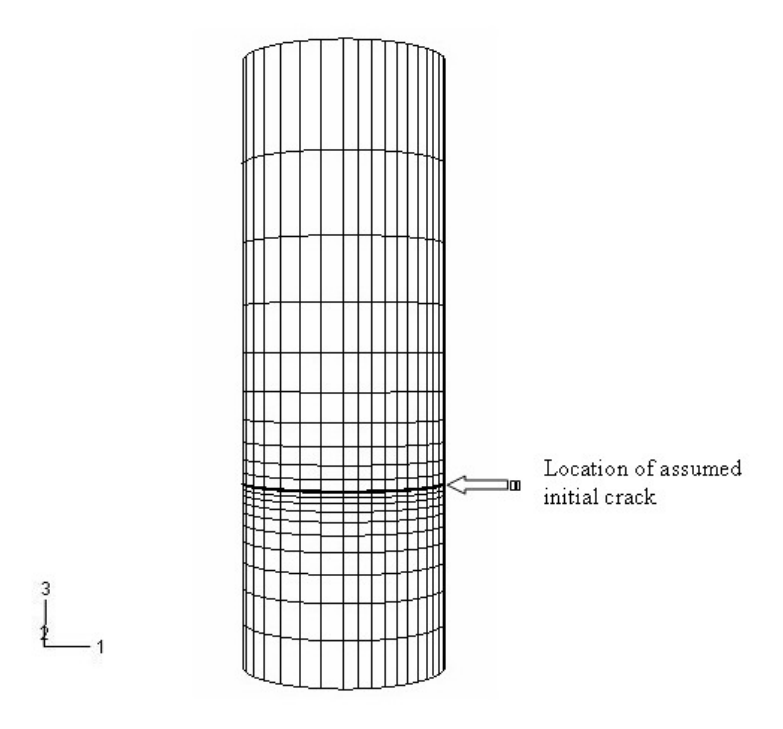


Figure 5.3: 3D-submodel of tubular connection containing though-wall cracked

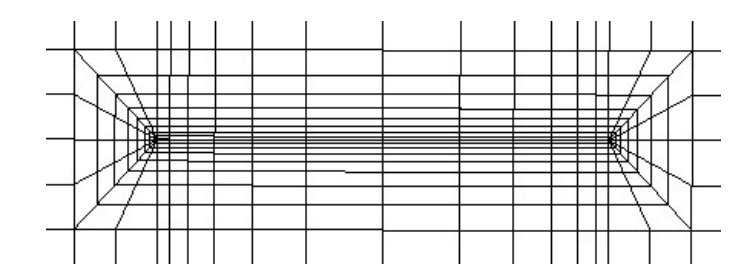


Figure 5.4: Finite element meshes in the crack tip region

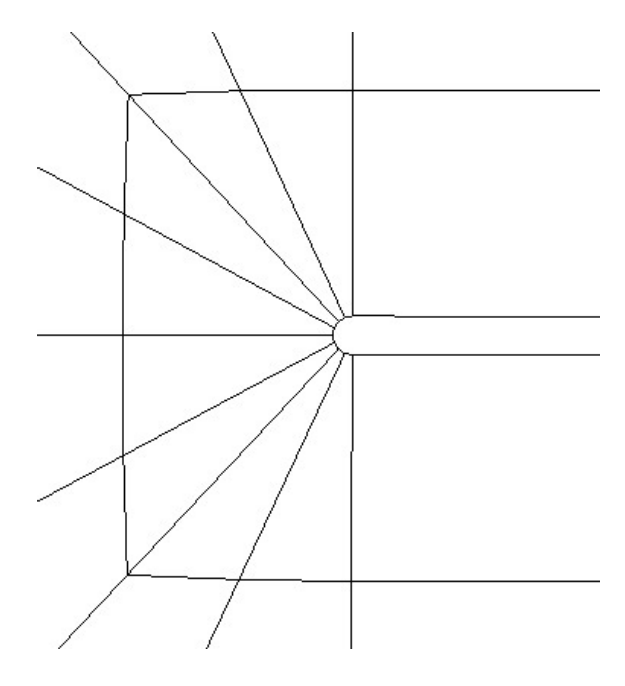


Figure 5.5: Finite element meshes in the crack tip region (zoom)

The dimensions of the tubular joint are 2.134 m diameter and 30 cm and 31 cm for the thickness of the top part and the bottom part of the connection respectively. In order to study the effect of initial crack length on applied CTOD and stress distribution pattern, five initial crack lengths, i.e. no crack, 2.5 cm, 5 cm, 10 cm and 33 cm, were assumed to locate in the global X direction (the direction of applied wave loading). Table 5.1 shows the number of nodes and elements in each sub model.

Table 5.1: Number of nodes and elements used in sub model

Crack length (cm)	No. of nodes	No. of elements
No Crack (NC)	620	600
2.5	1423	1360
5	1651	1576
10	1675	1600
33	2631	2512

5.2 Adding 3D-submodel into FE model of brace caisson (Combined model)

Finally, the sub models were placed into the global model by using distributing coupling elements (DCOUP3D) introduced with ABAQUS/Standard in the area of connection between the shell elements of the sub model and the beam elements of the global model. This special option offer general capabilities for transmitting loads and associating motions between one node and a collection of "coupling" nodes. The option associates the coupling nodes with a single node in a "rigid body" sense; translations and rotations of the node (the distributing coupling element node) are associated with the coupling node group as a whole. Figure 5.6 shows the complete FE model of brace caisson. Finally, Stokes' 5th order theory was applied to the combined model in the global X direction.

5.3 Analyses results

5.3.1 Natural frequencies extraction of the brace caisson (Combined model)

In order to check the compatibility of 3D-submodel in the global FE model, the natural frequencies extration were performed and compared with the original FE model. The results were shown in Table 5.2.



Figure 5.6: FE model of brace caisson including 3D-submodel of cracked connection (Combined model)

Table 5.2: Comparison of natural frequencies between original FE model and combined FE model

Crack length (cm)	Natural frequncies (Hz)		
	1 st Mode	2^{nd} Mode	3^{rd} Mode
Original FE model	0.62431	0.80599	1.3720
No Crack (NC)	0.62318	0.80339	1.3717
2.5	0.62398	0.80523	1.3719
5	0.62415	0.80561	1.3719
10	0.62417	0.80566	1.3719
33	0.62411	0.80554	1.3719

It can be seen that the first three natural frequencies of the combined model show good agreement with the results from original FE model. Figure 5.7 shows the first three mode shapes of vibration of combined model. Again it shows good agreement with the original FE model.

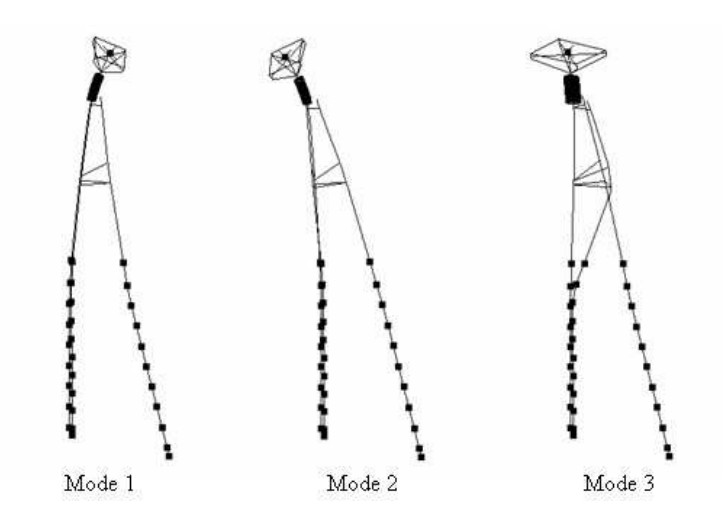


Figure 5.7: Mode shapes of vibration for base case at S.W.L. of combined model

5.3.2 Applied CTOD measurements from Sub Model Analyses

There are two common ways to define the crack tip opening displacement (CTOD), δ , namely the displacement at the original crack tip and the 90° intercept as shown in Figure 5.8.

The 90 $^{\circ}$ intercept is widely used to investigate CTOD in finite element measurements. The achievement of the CTOD is to provide a measure of crack tip severity

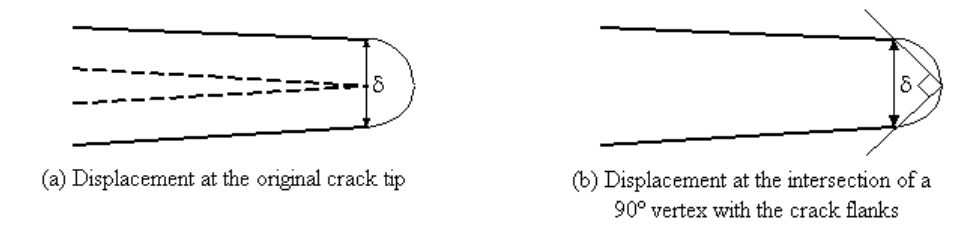


Figure 5.8: Definitions of CTOD [2]

Table 5.3: Effects of material preperties on the applied CTOD values

	Elastic CTOD (mm)		Elastic-Plastic	
Crack length (cm)			(cm) CTOD (mm) CTOD (mm)	
	Left	Right	Left	Right
2.5	0.00392	0.00393	0.017	0.017
5	0.00661	0.00664	0.0224	0.0225
10	0.00889	0.00896	0.04	0.041
33	0.0216	0.0220	0.12	0.125

throughout the whole plane-strain, elastic-plastic, and fully plastic behaviour regions, while K_I is measured only in the elastic plane-strain region or approximately in the early part of the elastic-plastic region. Hence, this section presents the results of applied CTOD measurements from the finite element analyses.

Table 5.3 shows the comparison of the applied CTOD values. It can be seen that the applied CTOD increases proportionally with the crack length. The maximum CTOD, i.e 0.13 mm, occurs when crack length equal to 33 cm. Comparison of the applied CTOD values between assumed elastic and elastic-plastic properties, the significant increases of CTOD can be obtained by the factor around 5.

Figure 5.9 shows the plot of circumferential stress of the tubular joint. It can be seen that highest stress occurs at the crack tip region for all cases. Meanwhile the lowest stress occurs at the area approximately 90° measured from crack tip in both clockwise and anti-clockwise directions after that stress starts to rise toward the back of the tubular joint.

5.3.3 Practical assessment methods for though-wall crack in minimum structures

These analyses attempt to represent the real situation by simplified treatment to provide guidance on practical assessment methods. In general, full scale dynamic finite analyses are time consuming and high performance computing facilities are

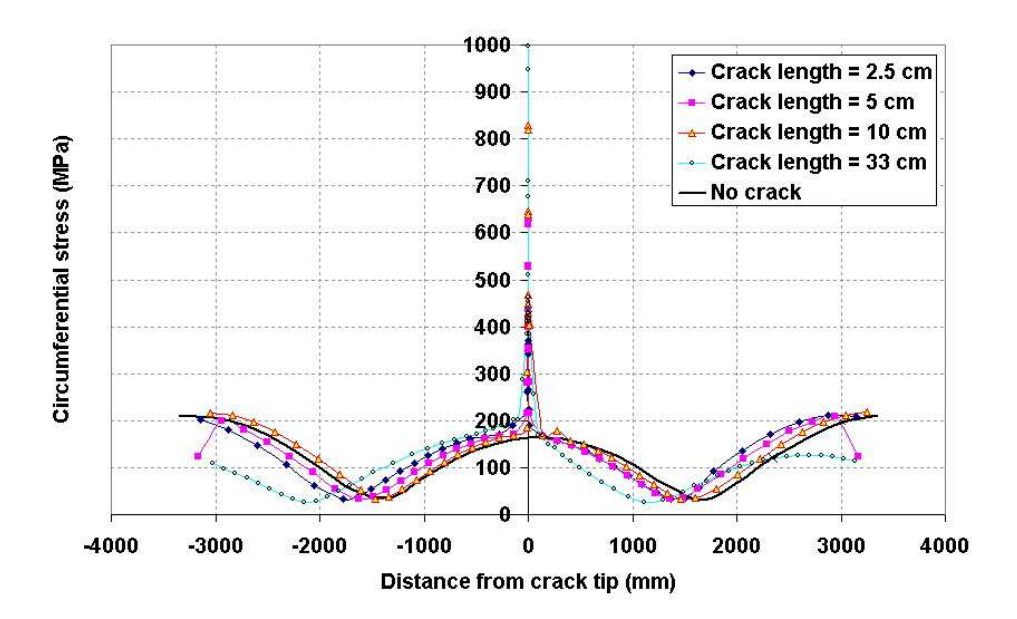


Figure 5.9: Stress distribution around the circumferential of the tubular joint

required which are beyond the scope of conventional designers. Thus, a simplified method for estimating the performance of the tubular connection is introduced in this study. The results from the approximate method are then compared with those obtained from full dynamic FE analyses.

From the point of view of assessment of structural integrity of structures containing cracked, a close approximation to the practical side of the problem can be obtained from the fracture mechanics assessment. When the maximum stresses at the members are below yield strength or contained by elastic regions, the stress-based concepts can be used in the assessment of safety critical components. The BSI Document PD 6493 [30] has been most widely used by following that procedure and is a major part of the latest version of that code given in BS7910 [7]. The applied stress intensity factor, K_I , has the following general form:

$$K_I = (Y\sigma)\sqrt{\pi a} \tag{5.1}$$

where

$$Y\sigma = M f_w M_m \sigma_{max} \tag{5.2}$$

and where a is half flaw length of through-thickness flaw; M is bulging correction factor; f_w is finite width correction factor; σ_{max} is the maximum tensile stress; M_m is a stress intensity magnification factor.

The applied CTOD, δ_I , is determined from K_I as follows:

• for steels (including stainless steels) and aluminium alloys where $\sigma_{max}/\sigma_y \leq$ 0.5, and for all σ_{max}/σ_y ratios with other materials:

$$\delta_I = \frac{K_I^2}{\sigma_y E} \tag{5.3}$$

• for steels (including stainless steels) and aluminium alloys where $\sigma_{max}/\sigma_{y} > 0.5$:

$$\delta_I = \frac{K_I^2}{\sigma_y E} \left(\frac{\sigma_y}{\sigma_{max}}\right)^2 \left(\frac{\sigma_{max}}{\sigma_y} - 0.25\right) \tag{5.4}$$

where σ_y is yield strength of the material and E is modulus of elasticity of the material.

By using the above equation, a simplified method for assessing the crack tip severity can be done by performing the following procedure:

- Step 1: Perform dynamic time history analyses on a simple brace caisson model sujected to wave loading (model containing only beam element)
- Step 2: Extract the maximum stress value from the critical connection.
- Step 3: Substitute all data in either Equation (5.3) or Equation (5.4) depending on σ_{max}/σ_y ratio.

Table 5.4: Comparison of the applied CTOD values

Crack length (cm)	CTOD (mm)		
	Submodel Analyses	Simplified analyses	
2.5	0.017	0.0193	
5	0.0225	0.0306	
10	0.041	0.0548	
33	0.125	0.145	

From a simplified FE analysis, the stress level at the same connection, as in the sub model analyses, was extracted from the the original FE model which was taken as 200 MPa. It could be seen that the ratio between σ_{max}/σ_y is equal to 0.5. Hence, Equation (5.3) was used to perform the simplified analyses.

By applying the simplified method, the applied CTOD for different crack lengths can be predicted as summarized in Table 5.4. The results in Table 5.4 are considered as the critical approximation of applied CTOD. It can be seen that the results of applied CTOD give a good agreement with the FE results of sub model analyses. Hence, this method can enormously reduce the analysis time which allows design engineers to assess the possibility of connection fractures, or determine approximate values of toughness and defect size requirements for given peak stress levels.

5.4 Closing Remarks

In this chapter, the analyses were conducted to investigate the factors that contributed to failure of the welded connections. Two parameters were considered for assessing the performance of modified connections. The results revealed the general increase in severity of conditions toward the crack tip. The stress distribution also confirmed that the position of the maximum stress coincided with the location of the fracture initiation. The material tensile properties also affect the crack tip severity at the crack tip.

Finally, The applied CTOD values obtained from a simplified method showed a

good agreement with the FE results of sub model analyses. Therefore, this method can enormously reduce the analysis time which allows design engineers to assess the possibility of connection fractures, or determine approximate values of toughness and defect size requirements for given peak stress levels.

Chapter 6

Conclusions

The primary goals of this study were to give guidance on the braced caisson behaviour under wave loading. A better understanding of the wave loading effects on the global behaviour of structures has been gained from the present work. The main points highlighted in this work are:

- Reviewing the typical offshore structure found in the industry. In this part, literature reviews have been done to classify the type of offshore structure.
- Describing the modeling technique of wave loading and their effects on offshore structure were also investigated.
- Obtaining the displacement response of the braced caisson under different influential parameters, including wave height, wave velocity and wave period. From this study, it can be seen that the wave velocity has little effect on the response of braced caisson while wave height and wave period have more effect. Decreasing wave height reduces the peak response of braced caisson at the same level of reduction. Changing of the wave period also affect the response of braced caisson. Decreasing in the wave period reduce the peak response in all cases except when the frequency of wave loading matches the natural frequency, and this gives higher response.
- Describing the braced caisson behaviour using Wavelet analyses. From this

study, the response of braced caisson can be explained into time-frequency domain using Wavelet analysis. The peak of the spectrum of the caisson corresponds with the peak of the applied wave. Firstly, the braced caisson moves with the combination of low and high frequencies. After that the amplitude of low frequency part will decay while high frequency part remains uniform. These means that the caisson has the small vibration during the whole movement of the caisson. Results of changing the wave height (controlled wave velocity and wave period) show the spectrum gives the same trend as the previous case but with smaller amplitude.

• An engineering approach to the assessment method for through-wall crack in minimum structures subjected to wave loading has been presented in submodel analyses. The applied CTOD values could be obtained. Changing the assumed material properties affected the CTOD output. Finally, a simplified method for assessing the crack tip severity was introduced. The applied CTOD values obtained from a simplified method showed a good agreement with the FE results of sub model analyses. Therefore, this method can enormously reduce the analysis time which allows design engineers to assess the possibility of connection fractures, or determine approximate values of toughness and defect size requirements for given peak stress levels.

Bibliography

- [1] HKS 1998. ABAQUS User's Manual Version 5.8. The HKS Plc.
- [2] T. L. Anderson. Fracture Mechanics: Fundamentals and Applications. CRC Press, London, 1995.
- [3] Atkins. Dynamics of Marine Structures: Methods of Calculating the Dynamic Response of Fixed Structures Subject to Wave and Current Action. Atkins Research & Development, UK, 1977.
- [4] J. M. Barsom and S. T. Rolfe. Fracture and Fatigue Control in Structures Applications of Fracture Mechanics. Prentice Hall, Inc., Englewood Cliffs, NJ, 1987.
- [5] Walker S. Brebbia C.A. Dynamic Analysis of Offshore Structures. Butterworth&Co. Publishers Ltd, UK, 1979.
- [6] BS6729:1987. Determination of the dynamic fracture toughness of metallic materials. British Standard Institution, London, 1987.
- [7] BS7910:1999. Guide on methods for assessing the acceptibility of flows in fusion welded structures. British Standard Institution, London, 2000.
- [8] F. M. Burdekin and D. E. W. Stone. The Crack Opening Displacement Approach to Fracture Mechanics in Yielding Materials. *Journal of Strain Analysis*, 1:145–153, 1966.

- [9] C.S. Burrus, R.A. Gopinath, and H. Guo. Introduction to Wavelets and Wavelet Transforms, a Primer. Prentice Hall, Upper Saddle River, NJ (USA), 1998.
- [10] M. G. Dawes. An Introduction to K, CTOD and J Fracture Mechanics Analyses and Toughness, and the Application of These to Metal Structures. TWI Report No. 577/1996, TWI, UK, 1996.
- [11] R. Dodds, A. Gullerud, K. Koppenhoefer, and C. Ruggieri. Warp3d-release 13: 3-D Dynamic Nonlinear Fracture Analysis of Solids Using Parallel Computers and Workstations. Structural Research Series 607, UILU-ENG-95-2012, University of Illinois at Urbana-Champaign, 1999.
- [12] J. J. Duga, W. H. Fisher, R. W. Buxbaum, A. R. Rosenfield, A. R. Bush, E. J. Honton, and S. C. McMillan. The Economic Effects of Fracture in the United States. NBS Special Publication 647-2, United States, Washington, DC, Department of Commerce, March 1983.
- [13] D. S. Dugale. Yielding of Steel Sheets Containing Slits. J. Mech Phys Sol, 8:100–108, 1960.
- [14] ASTM E399. Standard Test Method for Plane-Strain Fracture Toughness of Metallic Materials. ASTM, USA, 1990.
- [15] PDA Engineering. PATRAN V9.0 User Manual. USA, 1993.
- [16] ESIS-P2. ESIS Procedure for Determining Fracture Behaviour of Materials. European Structural Integrity Society (ESIS), 1992.
- [17] A. A. Griffith. The Phenomena of Rupture and Flaw in Solids. Transactions, Royal Society of London, A-221:163–198, 1920.
- [18] American Petroleum Institute. API recommended practice 2A 20th edition, and supplement 1. American Petroleum Institute, Washington, DC, USA, 1996.

- [19] G. R. Irwin. Analysis of Stresses and Strains Near the End of a Crack Traversing a Plate. Transaction, ASME, Journal of Applied Mechanics, 24:361–364, 1957.
- [20] G.R. Irwin. Plastic Zone Near a Crack and Fracture Toughness. 1960 Sagamore Ordance Materials Conference, Syracuse University, 1961.
- [21] G.R. Irwin. Linear Fracture Mechanics, Fracture Transition, and Fracture Control. Engineering Fracture Mechanics, 1(2):241–257, August 1968.
- [22] Oil & Gas Journal. Developing Marginal Offshore Fields. *International Petroleum News and Technology*, 93(29):33–49, 1995.
- [23] John D. Landes and Donald E. McCabe. Load History Effects on the J_R -Curve. ASTM STP 803, pages 723–738, 1981.
- [24] F. Z. Li, C. F. Shih, and A. Needleman. A Comparison of Methods for Calculating Energy Release Rates. *Engineering Fracture Mechanics*, 21:405–421, 1985.
- [25] D. P. Miannay. Fracture Mechanics. Springer-Verlag, New York, 1998.
- [26] Johnson J.W. Schaaf S.A. Morison J.R., O'Brien M.P. The force exerted by surface waves on piles. *Petrol. Trans.*, *AIME*, 189, 1950.
- [27] MSL. JIP comparative evaluation of minimum structures and jackets: Effect of vessel impact on intact and damaged structures. Doc Ref C209R007 Rev1, MSL Engineering Limited, Ascot, UK, 1999.
- [28] T. Nakamura, C. F. Shih, and L. B. Fround. Analysis of a Dynamically Loaded Three-Point-Bend Ductile Fracture Specimen. Engineering Fracture Mechanics, 25:323–339, 1986.

- [29] G. P. Nikishkov and S. N. Atluri. Calculation of Fracture Mechanics Parameters for an Arbitrary Three-Dimensional Crack, by the 'Equivalent Domain Integral' Method. *International Journal of Numerical Methods in Engineering*, 24:1801– 1827, 1987.
- [30] PD6493:1991. Guidance on methods for assessing the acceptibility of flows in fusion welded structures. British Standard Institution, London, 1991.
- [31] Ramboll. JIP Comparative Evaluation of Minimum Structures and Jackets, Issue 6, Document Ref: AM7565/JIPAGR. Atkins Research & Development, Surrey, UK, 1998.
- [32] J. R. Rice. A Path Independent Integral and the Approximate Analysis of Strain Concentration by Notches and Cracks. *Journal of Applied Mechanics*, 35(6):379–386, jul 1968.
- [33] Ultiguide. Best Practice Guidelines for Use of Non-linear Analysis Methods in Documentation of Ultimate Limit States for Jacket Type of Offshore Structures. Det Norske Veritas, Norway, 1999.
- [34] A. A. Wells. Unstable Crack Propagation in Metals:Clevage and Fast Fracture.

 Proceeding of Crack Propagation Symposium, Cranfield, 1:210–230, 1961.
- [35] H. M. Westergaard. Bearing Pressures and Cracks. *Transaction, ASME, Journal of Applied Mechanics*, pages 49–53, 1939.

Appendix A

Outputs and Manuscript

1. Publications

- K. Kuntiyawichai, S. Chucheepsakul and M.M.K.Lee, 2004, "Analysis of offshore structures subjected to various types of sea wave", 23rd International Conference on Offshore Mechanics and Arctic Engineering (OMAE2004), 20-25 June 2004, Vancouver, CANADA.
- K. Kuntiyawichai and S. Chucheepsakul, 2005, "Assessment of through-wall crack in Minimum structures subjected to wave loading", Submitted to Engineering Structures (IF = 0.809)

2. Benefits from this work

- The present study provides a simplified method for offshore design engineers to evaluate critical conditions in the connections.
- A technical guidance on the offshore design under dynamic loading especially wave loading can be obtained from this study.

Manuscript

K. Kuntiyawichai, S. Chucheepsakul and M.M.K.Lee, 2004, "Analysis of offshore structures subjected to various types of sea wave", 23rd International Conference on Offshore Mechanics and Arctic Engineering (OMAE2004), 20-25 June 2004, Vancouver, CANADA.

OMAE2004-51040

ANALYSIS OF OFFSHORE STRUCTURES SUBJECTED TO VARIOUS TYPES OF SEA WAVE

K. KUNTIYAWICHAI

DEPARTMENT OF CIVIL ENGINEERING UBONRATCHATHANI UNIVERSITY UBONRATCHATHANI THAILAND, 34190 Email: kittisak.k@ubu.ac.th

S. CHUCHEEPSAKUL

DEPARTMENT OF CIVIL ENGINEERING KING MONGKUT'S UNIVERSITY OF TECHNOLOGY THONBURI BANGKOK, THAILAND, 10140 Email: somchai.chu@kmutt.ac.th

M.M.K. LEE

SCHOOL OF CIVIL ENGINEERING AND THE ENVIRONMENT UNIVERSITY OF SOUTHAMTON SOUTHAMTON, SO17 1BJ, UK Email: M.M.K.Lee@soton.ac.uk

ABSTRACT

The principal aim of this paper is to study the dynamic behaviour of offshore platforms subjected to wave loading. A general review of offshore structure, wave loading and their effects on offshore structures are presented. A brief review on the basics of Wavelet analysis is also mentioned in this study. The techniques for modeling wave loading in finite element analyses are described and discussed in detail. A series of 3D analyses were carried out using the ABAQUS finite element software to study the effects on the dynamic response of the change in support conditions at the seabed. The effects of wave height, wave period and wave velocity on platform behaviour were studied. The results from time history analysis are characterized using Wavelet Analysis in order to obtain the response pattern due to wave loading. These analyses allow the frequency response of the jacket structures to be described in the time domain. These results give a clear view on the response of jacket structure. The important parameters on offshore modeling have also been identified and discussed in this paper. The results presented in this study can be used as a guidance for engineer in order to understand the dynamic behaviour of jacket structures subjected to wave loading.

INTRODUCTION

In general, dynamic analysis involves the determination of the response of a structure or component which is subjected to forces or displacements that vary with time. There are many types of dynamic loading, such as those produced by waves, blasts, cranes, traffics, earthquakes etc.

Wave loading may cause serious structural damage. A study of this leads to a better understanding of structural dynamics and their effects on structures. Therefore, a better understanding of the dynamic behaviour of offshore structures has become a very important task for dealing with dynamic loading.

One of the most important parameters associated with structural vibration is the natural frequency. Each structure has its own natural frequencies which control its dynamic behaviour. When a natural frequency of vibration of a structure coincides with the frequency of the external dynamic loading, it will lead to excessive deflections and potential catastrophic failures. This phenomenon is known as *resonance*. An example of a structural failure under dynamic loading is the very well known collapse of the Tacoma Narrows Bridge during wind-induced vibration. This present study will focus on the dynamic response of braced caisson subjected to wave loading.

GENERAL REVIEWS OF OFFSHORE STRUCTURE

Offshore structures are used for a variety of reasons [1]:

- Oil and gas exploration
- Navigation aid towers
- Bridges and causeways
- Ship loading and unloading facilities

Offshore structures can be designed for installation in protected waters, such as lakes, rivers, and bays or in the open sea, many kilometers from shorelines. The oil and gas exploration platforms are some of the best examples of offshore structures that can be placed in water depths of 2 kilometers or more. These structures may be made of steel, or reinforced concrete or a combination of both. In the United States these offshore oil and gas platforms are generally made of various grades of steel, from mild to high strength (240 MPa to 360 Mpa yield). Within the category of steel platforms, there are various types depending on their use and the water depth in which they are situated. Therefore, offshore oil/gas exploration (and drilling) platforms can be of the following types.

- Converted Jackup barges
- Fixed tower structures
- Tension Leg platforms (TLPs)
- Stationary floating SPARs

Each of these types is chosen primarily due to water depth considerations, and secondarily due to the intended service and quantity of deck equipment necessary to perform its service.

- The Converted jackup barges are the rarest, and may be used in remote areas with relatively shallow water depths. Chevron uses some offshore Congo in the Lukami field, for example.
- The fixed tower structures are the most common offshore structure found in Louisiana and Texas coasts in the Gulf of Mexico, and the North Sea. These structures vary in size and height, and can be used in water depths of up to about 300 meters, although most commonly in water depths of less than 150 meters. Within this category there are 4-leg, 6-leg, and 8-leg towers and also minimal structures whose decks are supported by a single unbraced or pile-braced caisson as shown in Fig. 1. Minimal structures are used in water depths of less than 50 meters. The single caisson types of minimal structures are also used as navigational aid towers in rivers and bays.
- The Tension Leg Platforms are used in water depths greater than 300 meters. They consist of a floating deck structure anchored to pile heads on the sea floor by means of long pipes which are always kept in tension, and thus can be flexible without risk of a column buckling collapse failure due to very high Kl/r ratios. (The slenderness of columns is indicated by the Kl/r ratio; the higher the ratio, the lower the compression allowable stress.)
- The SPAR platforms are used in very deep water exploration, even in the Gulf of Mexico area, beyond

the continental shelf. The SPAR is a vertical floating cylinder attached, by means of cables, to anchors placed on the seafloor more than a kilometer away.

WAVE LOADING

Waves are normally generated by wind blowing over the water surface and continue to exist after the wind has ceased to affect them. For offshore structures, dynamic response due to wave loading is an important aspect that has to be included in design considerations.

In general, wave theories which are widely used with offshore structures are the Stokes'5th order theory and the Airy wave theory. The differences between the two theories lie in the wave properties, including wave height, water depth and wave period, as shown in Figs. 2 and 3. From Fig. 3 it can be seen that the Airy wave theory is generally used when the ratio of the wave height to the water depth is less than 0.03, provided that the water is deep (ratio of water depth to wavelength is greater than 20), whereas the Stokes' 5th order wave theory is a deep-water wave theory that is valid for relatively large wavelengths. For a structural member immersed in fluid e.g., offshore piping and riser problems, there are three types of force to be considered: drag forces via the Morison's equation [2], inertia loads, and buoyancy loads. Fluid drag is associated with velocities due to steady currents and any waves that may have been specified. Fluid inertia is associated with wave accelerations as shown in Eq. (1)

$$dF = \frac{1}{2}C_{D}\rho DU |U| ds + C_{M}\rho A\dot{U} ds$$
 (1)

where F is the total force in the direction of the water velocity and acceleration, U the velocity of the water at the center of the object, D the outer effective diameter of the cylinder, A the cross sectional area of the cylinder, ρ the fluid density , C_M the inertia coefficient, and C_D the drag coefficient. The modulus sign is used to ensure that the drag force changes sign with the velocity, rather than always acting in the same direction.

Buoyancy has two components [3]: the hydrostatic pressure measured to the mean fluid level and the dynamic pressure caused by the presence of waves. Partial submergence is done automatically for all fluid load types.

Drag and inertia loads are considered in two forms: distributed loads along the length of the element (distributed drag loading is further divided into a component normal to the element's axis and a component along the tangent to the element) and point drag and inertia loads where the beam changes cross-section.

Buoyancy loading is applied with a "closed-end" assumption; i.e. it is assumed that the element's ends can support buoyancy loading normal to the element's cross section. If the ends of the element are actually "open ended", i.e. the element's ends cannot support fluid pressure load points,

buoyancy forces are provided to remove the buoyancy forces at the ends of the element.

BASIC WAVELET ANALYSIS

Wavelets [4] are the mathematical functions that cut up data into different frequency components, and then study each component with a resolution matched to its scale. They have advantages over traditional Fourier methods in analyzing physical situations where the signal contains discontinuities and sharp spikes.

The wavelet analysis described here is known as the continuous wavelet transform or CWT. More formally it is written as:

$$\gamma(s,\tau) = \int f(t) \psi_{s,\tau}^*(t) dt$$
 (2)

where * denotes complex conjugation. This equation shows how a function f (t) is decomposed into a set of basis functions $\psi_{s,\infty}(t)$, called the wavelets. The variables s and τ are the new dimensions, scale and translation, after the wavelet transform.

The wavelets are generated from a single basic wavelet $\psi(t)$, the so-called *mother wavelet*, by scaling and translation:

$$\psi_{s,\tau}(t) = \frac{1}{\sqrt{s}} \psi\left(\frac{t-\tau}{s}\right) \tag{3}$$

In (3) s is the scale factor, τ is the translation factor and the factor $s^{-1/2}$ is for energy normalization across the different scales. From Eq. (3), it can be noted that low scale, s, give high frequency and high scale s, give low frequency. Substituting the definition in Eq. (3) into Eq. (2), then the *continuous Wavelet transform (CWT)* is

$$CWT(\tau, s) = \frac{1}{\sqrt{s}} \cdot \int h\left(\frac{t - \tau}{s}\right) \cdot s(t) \cdot d(t) \tag{4}$$

Form Equation (4), It can be seen that Wavelet transform performs decomposition of the signal using weight function h(t), which normally are complex functions called "mother Wavelet".

While the width and amplitude of short time Fourier transform basis functions are constant, Wavelet transform basis functions are more adaptable. Not only their widths but also their magnitudes are varied. The scale variables *a* can be varied to analyse a practical signal containing brief high frequency components and extended low frequency components. At low frequencies, high scales relatively longer in duration and small magnitudes are applied to cover low frequency components giving good frequency resolution but poor time resolution. At higher frequencies, reducing scales to relatively short duration

and increasing magnitudes give poorer frequency resolutions but higher time resolutions. Time-frequency plane of Wavelet transform and STFT are shown in Fig 4.

There are many different types of "Mother Wavelet" available. The choice of mother Wavelet function becomes an important factor. The best mother Wavelet is unclear for a particular application and an active area of research is to find optimal Wavelets for different applications, as shown in Fig. 5.

FINITE ELEMENT ANALYSES

The input data for the finite element models was generated by using the general purpose finite element package ABAQUS/AQUA [3] which contain the application of buoyancy, drag and inertia loads resulting from submersion in steady current, wave and wind. In addition, ABAQUS/AQUA is commonly used for the analysis of offshore structure and it enjoys a reputation for providing accurate elements and efficient solution routines [5-7].

• Description of the model.

A braced caisson is modelled in this study. The platform were designed by Ramboll according to API (1993), for the WS Atkins JIP "Comparative Evaluation of Minimum Structures and Jackets" (Atkins, 1998). This structure is defined in the fixed tower structure category. This platform has the total height of 52 metres from the seabed and a pile penetration of 48 metres. The top deck of the braced caisson has a 400 metric tons mass.

• Element selection

Three-dimensional, three-noded quadratic beam elements (as recommended in Ultiguide (1999) i.e. B32 available in ABAQUS, was used to model the platform tubular members. These elements have 16 integration points around the circumference. Each element was rigidly attached to each other.

• Material Properties

Material properties used for the FE model are as follows;

Young's modulus = $205 \times 10^9 \text{ N/m}^2$ Yield stress = $396.75 \times 10^6 \text{ N/m}^2$ Density of steel = 8242.75 kg/m^3

Boundary conditions

In order to investigate the boundary conditions at the seabed, three FE models with different boundary conditions were analysed. The finite element models for the braced caisson which with spring support and simplify boundary conditions at the seabed (pinned and fixed supported) are shown in Figs. 6 and 7, respectively. The FE model with spring support contains 253 elements and 183 nodes. Springs were attached down the length of the piles in the x, y and z-directions to represent the soil structure interaction that takes place between the pile and the foundations of the braced caisson. For the cases of simplify boundary conditions at the seabed, the FE model contains 62 elements and 169 nodes.

Analyses procedure

The present study is divided into three parts. The first part is to obtain the dynamic characteristics of the braced caisson under the different conditions summarized in Table 1. In each

case, the water level and wave velocity were varied. The second part of the analyses is to investigate the dynamic behaviour of the braced caisson under two types of sea wave, i.e. Airy wave theory and Stokes' 5th order theory. In this study, the effects of wave height, wave period and wave velocity on the response of the braced caisson were obtained. The range of each parameter considered in this study is shown in Table 2. Every parameter in Table 2 was considered in the analyses. For example, at wave height 16.4 m, each wave velocity and wave period on the list were investigated. The sequence was the same for all wave heights. The general direct time integration method called the Hilber-Hugues-Taylor operator, provided in ABAQUS/Standard [9], was used in the dynamic response analyses. The set of simultaneous nonlinear dynamic equilibrium equations was solved at each time increment. The solution was calculated by the Newton method. An automatic incrementation scheme provided in ABAQUS was also used in order to control the accuracy of the solution. Artificial damping call the ALPHA parameter was also introduced in the model. A value of $\alpha = -0.05$ was used because this introduced just enough artificial damping in the system to allow the automatic time stepping procedure to work smoothly.

Finally, the last part of the analyses is to analyze the response pattern of the braced caisson under different conditions using Wavelet analysis. With this analysis, the response patterns of the braced caisson can be described in the time-frequency domain.

RESULTS OF THE ANALYSES

This section presents the finite element results of the braced caisson analyses. The analyses were divided into two main parts, i.e. natural frequency calculations and dynamic response analyses under different influence parameters. The main purpose is to understand the basic dynamic behaviour of the braced caisson.

• Natural frequency calculations

Firstly, the first three modes of natural frequencies for braced caisson were determined under different boundary condition at the seabed, water level and steady current velocity. The results are shown in Tables 3-5 for the spring supported (called base case), the pinned supported and the fixed supported cases, respectively. It can be seen that the natural frequencies of the modified boundary conditions braced caisson differ from the base case (spring support) around 20% for both cases. These due to the effect of soil-structure interaction between soil and foundations of the braced caisson have been neglected. However, at the higher modes of vibration, the natural frequencies become closer to the base case. Fig. 8 show the example of the first three modes of natural frequency for braced caisson modeled with spring support. In the case of changing the sea level, it can be seen that increasing the sea levels reduce the natural frequencies of the braced caisson. This reduction occurs due to the damping from the S.W.L. In order to obtain the effect of steady current velocity on the natural frequency of the braced caisson, the

analysis was carried out at S.W.L. The results show that steady current velocity have no effect of the natural frequency of the caisson.

• Dynamic response analyses

In this part of study, two wave theories, Stokes' 5th order theory and Airy wave theory, were applied to the model. The criteria considered in this study, summarized in Table 2, are wave height, wave velocity and wave period. The results show that wave height and wave period affect the dynamic response of the braced caisson under Stokes'5th order theory but wave velocity appear to have less effects than the first two parameters, as shown in Figs. 9-11. Fig. 9 shows the displacement response of the braced caisson subjected to different steady current velocities (controlled wave height at 16.4 m and wave period at 12.6 sec). It can be seen that wave velocity has a small effect on the response of the brace caisson. In order to study the effect of wave height on the response of the brace caisson, four different level of wave height was considered for each wave theory. Fig. 10 illustrates the effect of wave height on the response of the braced caisson when Stokes' 5th order theory was applied (controlled wave velocity at 0.96 m/s and wave period at 12.6 sec). It can be seen that the peak responses at the top of the braced caisson reduce proportionally with the reduction of the wave height. If the wave period was changed while the other parameters were controlled, the responses of braced caisson are shown in Fig. 11. It can be seen that the spike of the response is shifted as the result of shorter wave period. For the case of 6.35 sec wave period, the response shows the highest peak because the frequency of the wave corresponds with the fourth mode natural frequency of the braced caisson.

Fig. 12 shows the displacement response of the braced caisson (base case with varying wave heights) subjected to Airy wave. The results show that the wave height has no effect on the response of the caisson because the wave height is very small compared with the water depth, i.e. 1~m << 34~m. For the case of changing wave velocity and wave period, the results, shown in Fig. 13), appear to be the same trend as changing wave heights.

Wavelet analyses of the response data

Finally, the responses from dynamic response analysis were analyzed using the Wavelet analysis and spectrum analyses. The results are shown in Figs. 14-18. First of all, spectrum analysis has to be done in order to get the frequency range of the response. Therefore, the displacement response data in time domain from Fig. 10 was analysed using Fast Fourier Transform (FFT) to get data in the frequency domain, as shown in Fig. 14. It can be seen that the braced caisson response within the frequency range between 0-1 Hz.

After that the displacement response data was analysed again using Wavelet analysis. In Fig.15, the x-, y and z-axes represent time, frequency scale and amplitude, respectively. From the principle of Wavelet analysis, low scale gives high frequency and low frequency high scale. Fig. 15 shows the response pattern of the braced caisson for the base case

subjected to a wave height of 16.4 m in time-frequency domain. It can be seen that the peak of the spectrum occurred corresponds with the peak of applied wave load. When the waves first strike the caisson, both low and high frequency occur due to the movement and vibration of the caisson, respectively. After that the amplitude of the low frequency part of the response decays. In contrast, the high frequency part of the response is uniform, which means that the caisson has the small vibration during the whole movement of the caisson. The Wavelet analyses were used to analyse other wave heights as shown in Figs. 16-18. It can be seen that decreasing wave height leads to decrease in amplitude of vibration within the high frequency range and increase in amplitude within the low frequency range.

CONCLUSION

The primary goals of this study were to give guidance on the braced caisson behaviour under wave loading. A better understanding of the wave loading effects on the global behaviour of structures has been gained from the present work. The main points highlighted in this work are:

- Reviewing the typical offshore structure found in the industry. In this part, literature reviews have been done to classify the type of offshore structure.
- Describing the modeling technique of wave loading and their effects on offshore structure were also investigated.
- Obtaining the displacement response of the braced caisson under different influential parameters, including wave height, wave velocity and wave period. From this study, it can be seen that the wave velocity has little effect on the response of braced caisson while wave height and wave period have more effect. Decreasing wave height reduces the peak response of braced caisson at the same level of reduction. Changing of the wave period also affect the response of braced caisson. Decreasing in the wave period reduce the peak response in all cases except when the frequency of wave loading matches the natural frequency, and this gives higher response.
- Describing the braced caisson behaviour using Wavelet analyses. From this study, the response of braced caisson can be explained into time-frequency domain using Wavelet analysis. The peak of the spectrum of the caisson corresponds with the peak of the applied wave. Firstly, the braced caisson moves with the combination of low and high frequencies. After that the amplitude of low frequency part will decay while high frequency part remains uniform. These means that the caisson has the small vibration during the whole movement of the caisson. Results of changing the wave height (controlled wave velocity and wave period) show the spectrum gives the same trend as the previous case but with smaller amplitude.

ACKNOWLEDGMENTS

The authors would like to acknowledge the financial support of the Thailand Research Fund (TRF) through Grant Number MRG4680060.

REFERENCES

- [1] American Petroleum Institute (1220 L Street, Northwest, Washington DC 20005 USA) RP-2A 20th edition, and supplement 1, dated December 1996.
- [2] Morison J.R., O'Brien M.P., Johnson J.W., Schaaf S.A. (1950) "The Force Exerted by Surface Waves on Piles", Petrol. Trans., AIME, Vol.189.
- [3] ABAQUS/AQUA (1999) User's Manuals Rev 5.5-5.8, Hibbit, Karlsson and Sorensen Inc., Rhode Island, USA.
- [4] Burrus, C.S., Gopinath, R.A., and Guo, H., INTRODUCTION TO WAVELETS AND WAVELET TRANSFORMS, A PRIMER. Upper Saddle River, NJ (USA): Prentice Hall. 1998.
- [5] HSE (1997) "Comparison of Reserve Strength Ratios of Old and New Platforms", Offshore Technology Report, OTO 97 046, Health & Safety Executive, Prepared by Brown & Root Ltd, pp 45-97
- [6] HSE (1999) "Dynamic Push-Over Analysis of Jacket Structures", Offshore Technology Report, OTO 98 092, Health & Safety Executive, Prepared by Mott MacDonald Oil Gas & Maritime Division
- [7] Ultiguide (1999) "Best Practice Guidelines for Use of Non-linear Analysis Methods in *Documentation of Ultimate Limit States for Jacket Type of Offshore Structures*", Published by Det Norske Veritas, Norway
- [8] Atkins (1998) "JIP Comparative Evaluation of Minimum Structures and Jackets", Issue 6, Document Ref:AM7565/JIPAGR, WS Atkins Science & Technology, Epsom, Surrey, England
- [9] ABAQUS (1998) Linear Dynamics with ABAQUS, Hibbit, Karlsson and Sorensen Inc., Rhode Island, USA
- [10] Oil & Gas Journal (1995) "Developing Marginal Offshore Fields", International Petroleum News and Technology, Vol 93, No. 29, pp 33-49

Table 1 Criteria for natural frequency analyses

Boundary Condition	Water Level	Steady current velocity
Spring supported	Dry	
(Base case)	+15 m	1.4 m/s
	+10 m	1.2 m/s
Pinned supported	+5 m	1.0 m/s
	S.W.L.	0.96 m/s
Fixed supported	-10 m	0.8 m/s
	-20 m	
	-30 m	

Table 2 Criteria for dynamic analyses

Type of wave theory	Wave height, m	Wave velocity, m/s	Wave period, sec
	16.4	1.4	12.6
Stokes' 5 th order	8.2	1.2	11.34
theory	6.56	1.0	10.08
	3.28	0.8	6.35
	1.0	1.4	12.6
Airy wave theory	0.8	1.2	11.34
	0.6	1.0	10.08
	0.4	0.8	6.35

Table 3 Natural frequencies of braced caisson (spring support)

***	Natural Frequency		
Water Level	1st Mode	2 nd Mode	3 rd Mode
Dry	0.62779	0.80859	1.4978
+15 m	0.61198	0.79488	1.3542
+10 m	0.61666	0.80001	1.3543
+5 m	0.62017	0.80293	1.3569
S.W.L.	0.62431	0.80599	1.3720
-10 m	0.62644	0.80757	1.4075
-20 m	0.62749	0.80834	1.4683
-30 m	0.62776	0.80856	1.4940

Table 4 Natural frequencies of braced caisson (pinned support)

***	Natural Frequency		
Water Level	1st Mode	2 nd Mode	3 rd Mode
Dry	0.75871	0.90959	1.5208
+15 m	0.74466	0.90002	1.3786
+10 m	0.74976	0.90491	1.3787
+5 m	0.75291	0.90684	1.3818
S.W.L.	0.75623	0.90845	1.3990
-10 m	0.75783	0.90919	1.4385
-20 m	0.75856	0.90952	1.5030
-30 m	0.75870	0.90958	1.5203

Table 5 Natural frequencies of braced caisson (fixed support)

***	Natural Frequency		
Water Level	1st Mode	2 nd Mode	3 rd Mode
Dry	0.76596	0.91294	2.4127
+15 m	0.75466	0.90457	2.0855
+10 m	0.75963	0.90947	2.0905
+5 m	0.76232	0.91127	2.1191
S.W.L.	0.76479	0.91249	2.1982
-10 m	0.76570	0.91287	2.2901
-20 m	0.76593	0.91293	2.3919
-30 m	0.76596	0.91294	2.4123



Figure 1 EDG Inc.'s Mantis I & II [10]

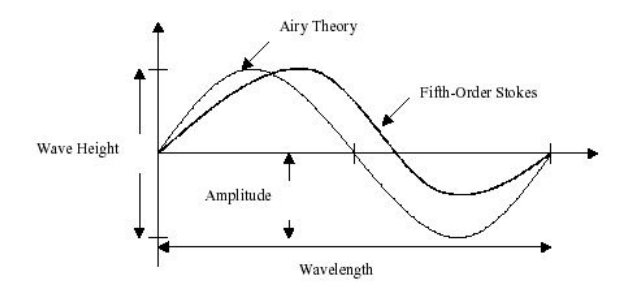


Figure 2 A comparison of wave theory [2]

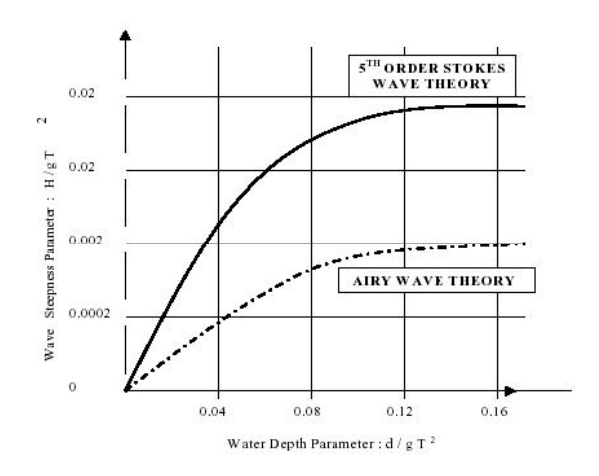


Figure 3 The limitation of Stokes' 5th order theory and Airy wave theory

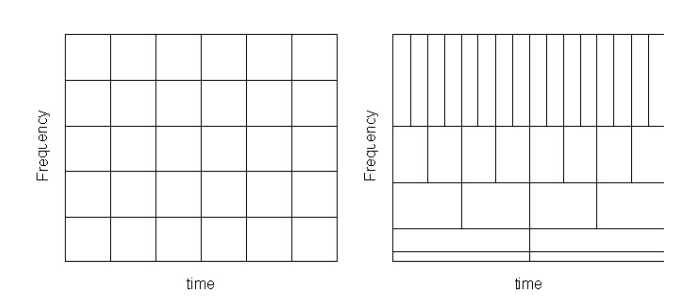


Figure 4 Time Frequency plane of STFT and Wavelet Transform

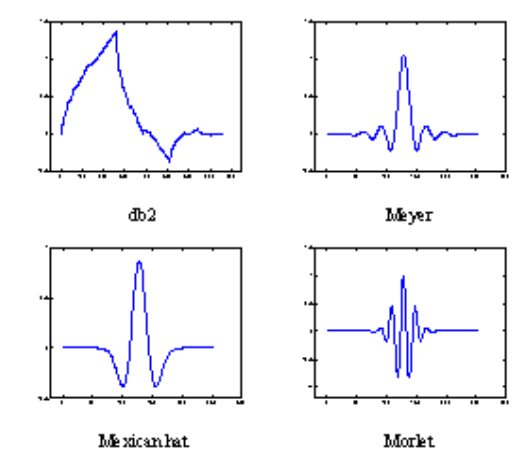


Figure 5 Some mother Wavelet functions.

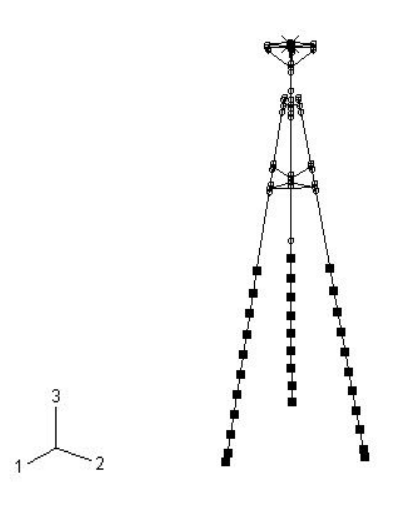


Figure 6 Finite element of brace caisson with spring support (base case).

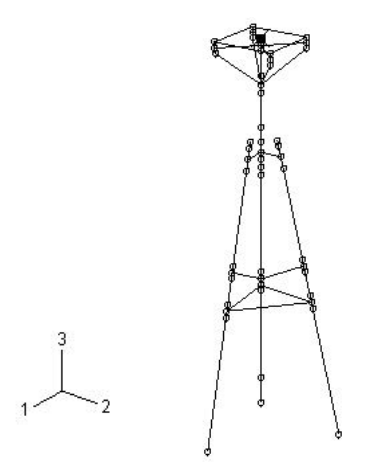


Figure 7 Finite element model of braced caisson with modify boundary condition at the seabed (fixed and pinned support).

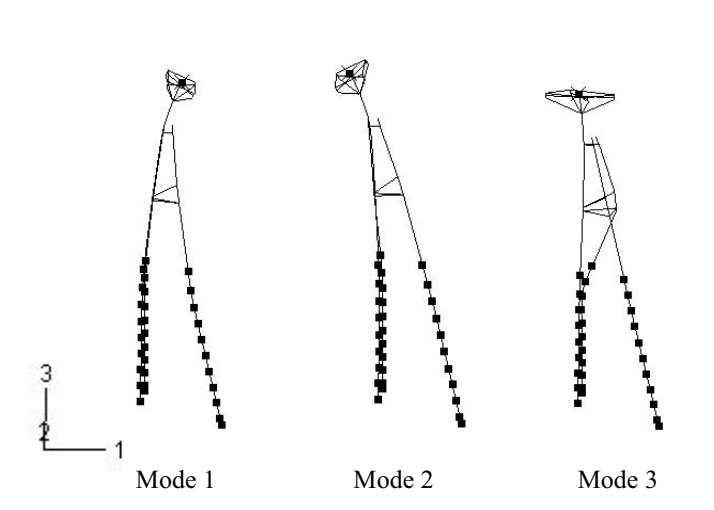


Figure 8 Mode shape of vibration for base case at S.W.L.

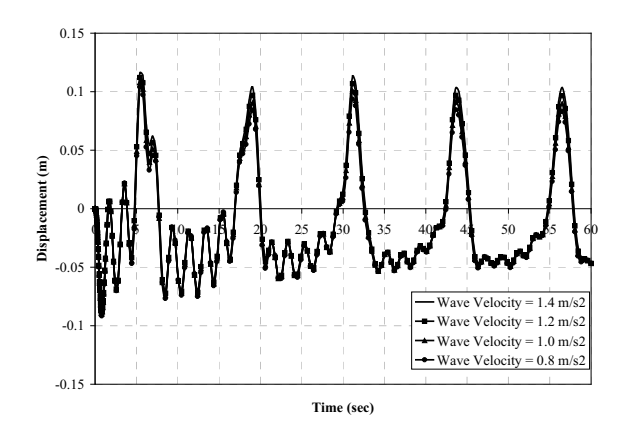


Figure 9 Dynamic response of braced caisson (wave height 16.4 m) subjected to Stokes' 5th order wave under different wave velocity

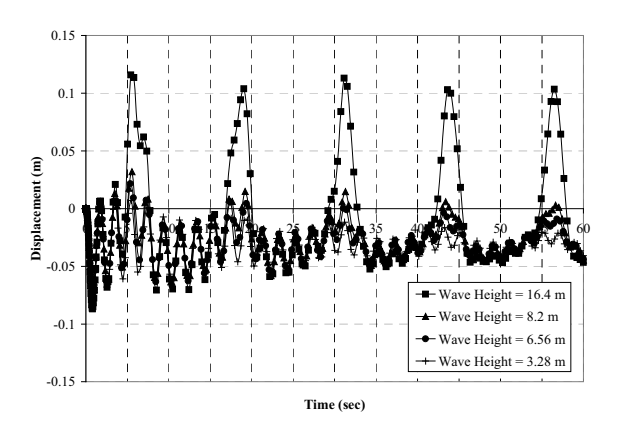


Figure 10 Dynamic response of braced caisson subjected to Stokes' 5th order wave under different wave height

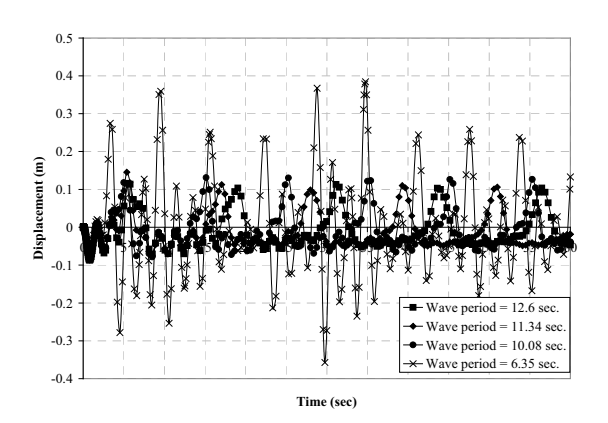


Figure 11 Dynamic response of braced caisson (wave height 16.4 m) subjected to Stokes' 5th order wave under different wave period

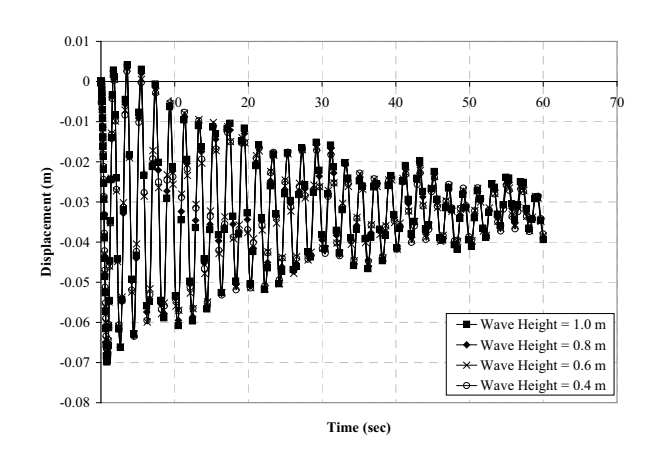


Figure 12 Dynamic response of braced caisson subjected to Airy wave under different wave height

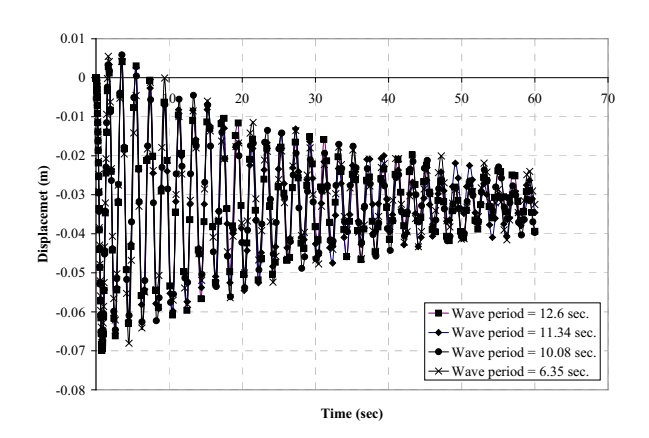


Figure 13 Dynamic response of braced caisson (wave height 16.4 m) subjected to Airy wave under different wave period

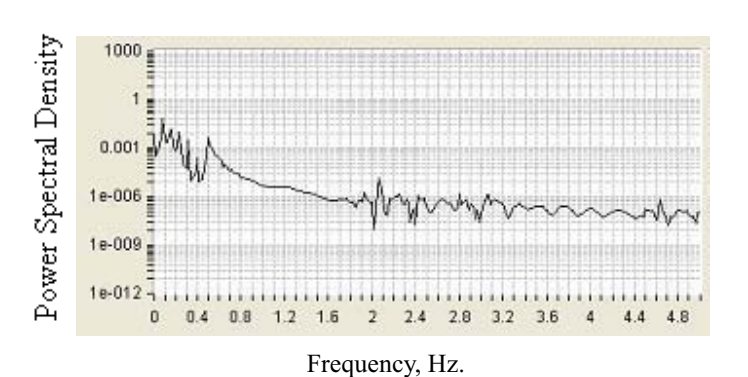


Figure 14 Power spectrum of displacement response data from Figure 10 (wave height = 16.4 m)

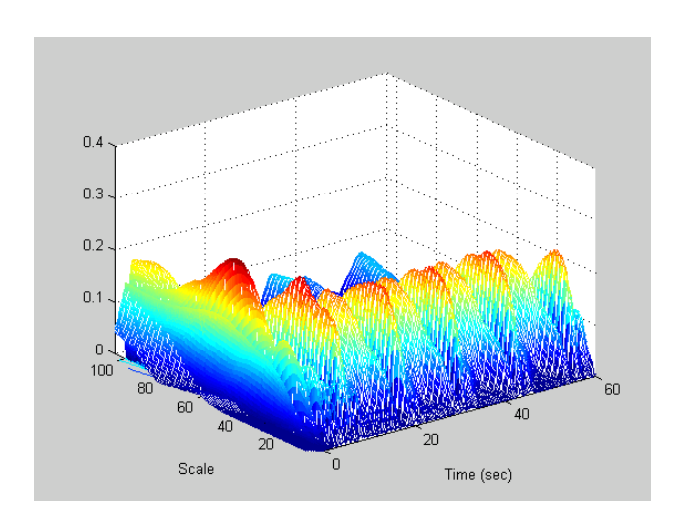


Figure 15 Wavelet analyses of displacement response data from Figure 10 (wave height = 16.4 m)

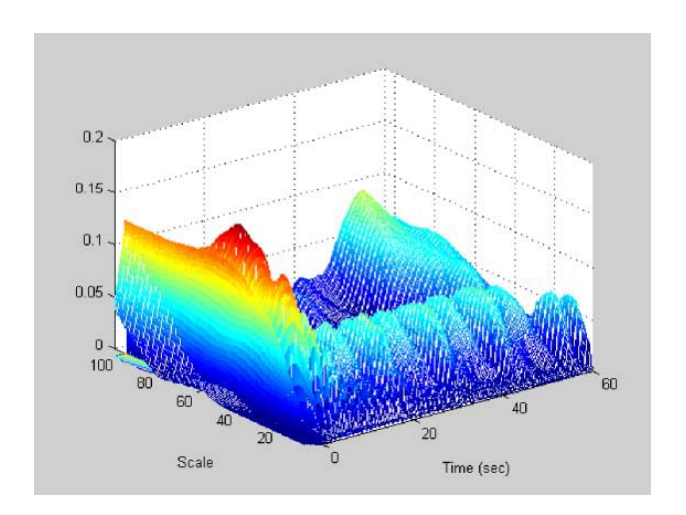


Figure 16 Wavelet analyses of displacement response data from Figure 10 (wave height = 8.2 m)

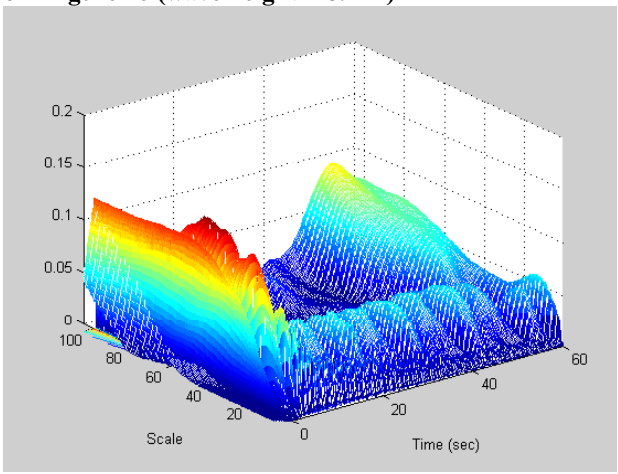


Figure 17 Wavelet analyses of displacement response data from Figure 10 (wave height = 6.56 m)

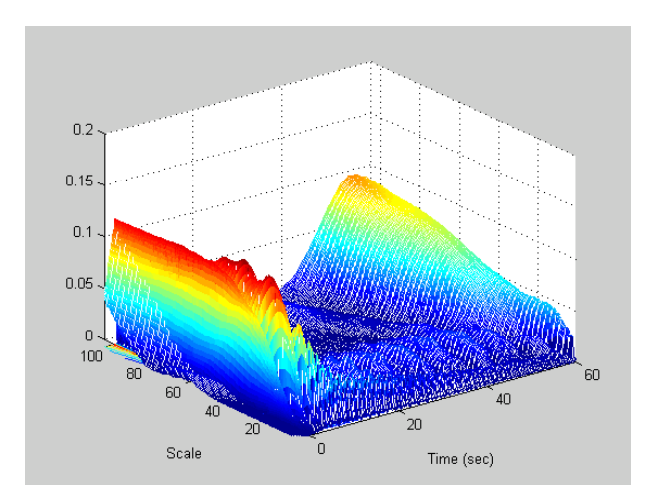


Figure 18 Wavelet analyses of displacement response data from Figure 10 (wave height = 3.28 m)